Auroral Arc Detection using a COTS Spectral Photometer for the Auroral Emission Radio Explorer (AERO) CubeSat Mission

by

Cadence Payne

B.S. Space Science
Morehead State University, 2017

Submitted to the Department of Aeronautics and Astronautics
in partial fulfillment of the requirements for the degree of

Master of Science in Aeronautics and Astronautics

at the

MASSACHUSETTS INSTITUTE OF TECHNOLOGY

May 2020

Author .....
Department of Aeronautics and Astronautics
May 19, 2020

Certified by .....
Kerri Cahoy
Associate Professor of Aeronautics and Astronautics
Thesis Supervisor

Accepted by .....
Sertac Karaman
Associate Professor of Aeronautics and Astronautics
Chairman, Graduate Program Committee

Auroral Arc Detection using a COTS Spectral Photometer for the Auroral Emission Radio Explorer (AERO) CubeSat Mission

by

Cadence Payne

Submitted to the Department of Aeronautics and Astronautics
on May 19, 2020, in partial fulfillment of the
requirements for the degree of
Master of Science in Aeronautics and Astronautics

Abstract

Auroral phenomena are dynamic in nature: observed events have rich structures that are both spatially and temporally complex, with scientifically interesting features. While optical auroral observations using CCDs or all-sky cameras are common, the aurora also have interesting emission properties at radio frequencies (RF), specifically in low-frequency and high-frequency bands.

The Auroral Emission Radio Observer (AERO) is a 6U CubeSat, equipped with a novel electromagnetic Vector Sensor (VS) antenna. The VS will target auroral emission in a measurement band from 100 kHz - 15 MHz, which enables the study of interesting emission types such as Auroral Kilometric Radiation (20 kHz -750 kHz), Medium Frequency Bursts (1.6 MHz - 4.4 MHz) and cyclotron emission (2.8 MHz - 3.0 MHz). The VS antenna measures 4-meters tip-to-tip once deployed from the CubeSat frame, and expands to form electric dipoles and magnetic loop antennas that are sensitive enough to probe this diverse set of science targets. Having a space-based platform, such as AERO's vector sensor antenna, positions the detector above the ionospheric plasma frequency which would otherwise limit observations of radio emissions.

Novel measurements from AERO's VS antenna require a set of contextual data to validate the fidelity of resulting data products. AERO includes a secondary payload referred to as an Auxiliary Sensor Package (ASP) that will augment VS measurements with contextual optical and magnetic data. The objective of AERO's contextual optical measurement is to detect the presence of auroral emission in multiple spectral bands, namely green-line emission at 557 nm and red-line emission at 630 nm. An AMS AG AS7262 6-channel visual band spectral photometer is selected as the optical sensor.

We present a radiometric model that evaluates the AS7262 sensor's ability to measure target auroral events. We consider a number of different test scenarios, including varying parameters such as auroral source radiance in units of Rayleigh, spacecraft

altitude, and others, to fully assess the sensor's ability to detect optical auroral signatures. The mission requirements include a minimum detection of 5 kR for the sensor to satisfy the optical measurement requirement. In our initial assessment, we find that the selected sensor in its current configuration may not be able to meet this requirement. In its current configuration, the sensor may be capable of detecting the presence of auroral events at high levels of intensity, in the over 100 kR range. The model developed in this work indicates that further analysis and possible modification to the front end optic or the sensor itself are needed. Though the radiometric model presented is tailored for the AS7262 sensor, it is easily adaptable to assess the performance of other auroral imagers. The contextual measurements provided by the ASP will contribute to the success of the AERO CubeSat mission in demonstrating that remote sensing techniques on CubeSat platforms can address unanswered questions about the aurora.

Thesis Supervisor: Kerri Cahoy
Title: Associate Professor of Aeronautics and Astronautics

Acknowledgments

First, I would like to thank my advisor Dr. Kerri Cahoy for her guidance and patience throughout my time in her group. She has been a strong source of encouragement and reassurance for me during this process, and I am honored to have her as a mentor.

I would also like to thank my colleagues and mentors at MIT's Haystack Observatory, namely Mary Knapp, Frank Lind, and Phil Erickson for their consistent positive reinforcement and unwavering support. This research would not have been possible without their contributions and thoughtful guidance. Additional thanks to my mentors Benjamin Malphrus and Thomas Pannuti at Morehead State University for providing me my first opportunity to work with Haystack. I truly appreciate your mentorship and willingness to continue to support me on my journey.

Special thanks to the AERO-VISTA team for making the process of building an incredibly complex CubeSat an enjoyable one. I would also like to thank Nicholas Belsten, a graduate student in our group for his contributions to this work.

To my mom, whose love and support I never have to question, and to my step father Sam who encouraged me to try out that first astronomy class in 2011. I cannot thank you all enough for how you continuously encourage and push me to keep expanding my goals.

Lastly, I would like to thank the members of the Space Telecommunications, Astronomy, and Radiation (STAR) lab, as well as my friends in the AeroAstro department for making my time here such an enjoyable experience. I'm looking forward to seeing you all again.

This project was supported by NASA's Heliophysics Technology and Instrument Development for Science (H-TIDeS), as well as the National GEM Consortium.

Per aspera ad astra!

THIS PAGE INTENTIONALLY LEFT BLANK

Contents

List of Figures

List of Tables

THIS PAGE INTENTIONALLY LEFT BLANK

Chapter 1

Introduction

The aurora borealis and australis are some of the most stunning atmospheric phenomena visible to the naked eye. Auroral optical emission is frequently surveyed in the visual regime as its properties are dynamic and intriguing. Auroral events are spatially and temporally rich, demonstrating complex structures and features that are still poorly understood [7]. The complexity of these visual representations of atmospheric molecular excitation makes observing auroral emissions important for understanding the dynamic interactions in the Earth-Sun system. In addition to fascinating optical characteristics, aurora also have interesting radio emissions in the Low-Frequency (LF) and High-Frequency (HF) bands, which are observable by radio remote sensing techniques. The Auroral Emission Radio Observer (AERO) is a 6U (roughly $10 \times 20 \times 30$ cm^3), NASA Heliophysics Technology and Instrument Development for Science (HTIDeS) CubeSat technology demonstration that will significantly increase our understanding of auroral radio emissions by surveying regions above the Earth's atmosphere in Low Earth Orbit (LEO). AERO's primary payload involves a novel Radio Frequency (RF) Vector Sensor (VS) antenna that observes low-frequency (100 kHz - 15 MHz) auroral radio emission. To support the VS radio emission measurements, AERO will also capture contextual optical emission data, providing confirmation that an auroral event was actually surveyed. This thesis focuses on the design, development, and testing of the Auxiliary Sensor Package (ASP) on AERO, in particular on the optical sensor. The objective of the optical auxiliary

sensor is not to image the aurora, but rather to serve as a binary (yes/no) detection technique to confirm the presence of auroral phenomena from intensity measurements across multiple sensor channels. A key contribution of this thesis is the development of tools to validate AERO's selected optical sensor, including a radiance budget that assesses the sensor's performance in observing auroral phenomena.

1.1 Motivation for an Auroral Observing CubeSat

Auroral phenomena are fascinating and have been surveyed for decades. Studying these dynamic events helps us understand the complex interactions between our Earth's magnetosphere, ionosphere, and the solar wind. Auroral observations improve our knowledge of energy coupling and plasma processes at the boundary between Earth and space [25]. The Earth's ionosphere can also affect the communication and navigation systems of spacecraft, which are of concern for both defense and commercial applications [25].

The aurora are frequently observed on the ground using cameras or all-sky imagers. Signatures from some of the more fine-scale emission types are weak and difficult to observe through the atmosphere. Low-frequency radio emissions (below 10 MHz) are difficult to measure due to observational limitations imposed on ground-based imagers that observe emission below the ionospheric plasma cutoff frequency [16]. At or near the ionospheric plasma frequency, the Earth's ionosphere behaves like an opaque shield that reflects emission with frequencies below the cutoff [24, 25]. There is great benefit in having 'eyes' in space to observe auroral generation, which occurs at altitudes of approximately 100 km for the auroral F-region. Both spatial and temporal coverage, as well as resolution are greatly increased with space-based remote sensing techniques compared with ground and sounding rocket based platforms [21, 25].

The CubeSat platform offers a low-cost approach for performing novel technology demonstrations, although it comes with limitations in Size, Weight and Power (SWaP). Missions that are willing to accept higher risk and the resource-constrained conditions can get to space at a lower cost and more quickly compared to larger

spacecraft.

The CubeSat platform should work well for the validation of AERO's novel VS antenna. Despite the benefits, integrating the large, 4-meter tip-to-tip VS antenna into a small CubeSat form factor poses unique design and operational challenges; however, details addressing these challenges are addressed in other work, and we focus here on the ASP and its optical sensor.

Large observers, such as the joint Institute of Space and Astronautical Science's (ISAS) and NASA's Geotail spacecraft, are large compared with the CubeSat form factor (2.2 m diameter and 1.6 m tall for Geotail), heavy (greater than 1000 kg for each observing spacecraft), and can cost on the order of tens to hundreds of millions of dollars [22]. In comparison, AERO's 6U MP6 CubeSat bus from NanoAvionics is approximately $20 \times 22 \times 34$ cm^3 and weighs less than 12 kg with the payload fully integrated. AERO will complement and extend observations from larger space-based missions like Geotail and the well-equipped ground observatories, as well as benefit from any concurrent observations for validation.

1.2 Auroral Radiometry Background

1.2.1 Generation of Optical Auroral Emission

Electron precipitation is due to atomic and molecular interaction with energetic particles, namely electrons and ions, that are injected into the Earth's atmosphere from the solar wind. The energetic particles get trapped along Earth's magnetic field lines. When they are released, they 'rain' down into the Earth's ionosphere where they collide with and excite neutral atmospheric molecules and atoms [11]. Once the excited particles relax back into their lower energy states, they produce photons that contribute to the generation of multiple types of auroral phenomena [11]. The photons correspond to spectral line emissions; there are sharp peaks of emission intensity located at specific wavelengths, dependent on the molecules involved in the collisional events. These emission lines can be thought of as fingerprints that help to identify

which molecules were excited by the incident high-energy electrons. Two key examples are the green oxygen line at 557 nm and red doublet observed at 630 nm [11]. These oxygen lines are the primary targets of interest for AERO's optical auxiliary sensor, and are discussed in further detail in Section 1.3.1.

When a visible auroral event occurs, it appears simultaneously at all points located within a region known as the auroral oval at around 70 degrees latitude on the night side [11]. The auroral oval region is centered around the Earth's geomagnetic Northern and Southern pole, and has a radius of 1500-2000 km depending on the intensity of solar activity [11, 9]. As an aside, optical emissions come from lower in the ionosphere compared to radio emission, which are the primary science targets of the AERO mission and its VS payload.

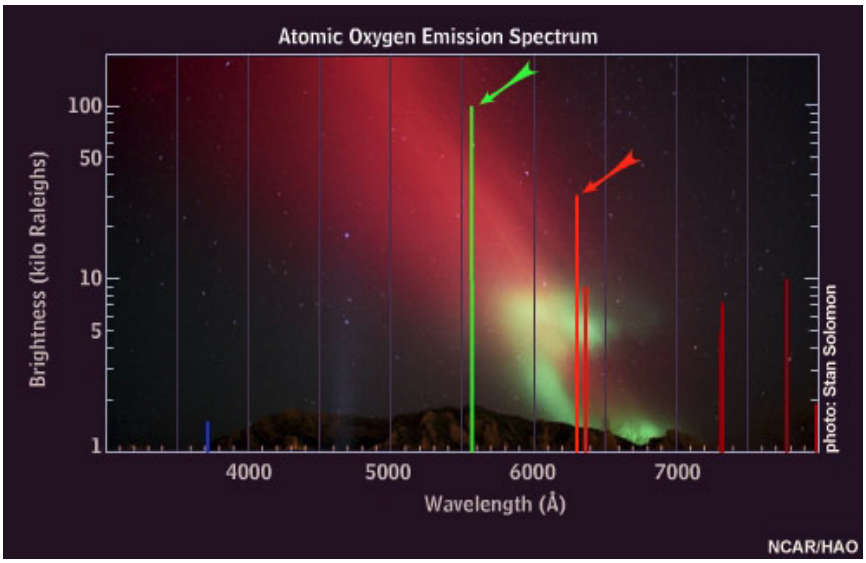

Figure 1-1: Spectrum of oxygen emission [26]

1.2.2 Target RF Auroral Emission Types

Auroral radio emissions in the low- and high-frequency (100 kHz - 15 MHz) range can be measured and provide insight to auroral ionospheric plasma conditions and processes [7]. Though there are hundreds of types of aurora, Auroral Kilometric Radiation (AKR) is one of the the most interesting and important types of auroral radio emission. AKR accounts for up to 1% of all radiated auroral energy [7]. AKR

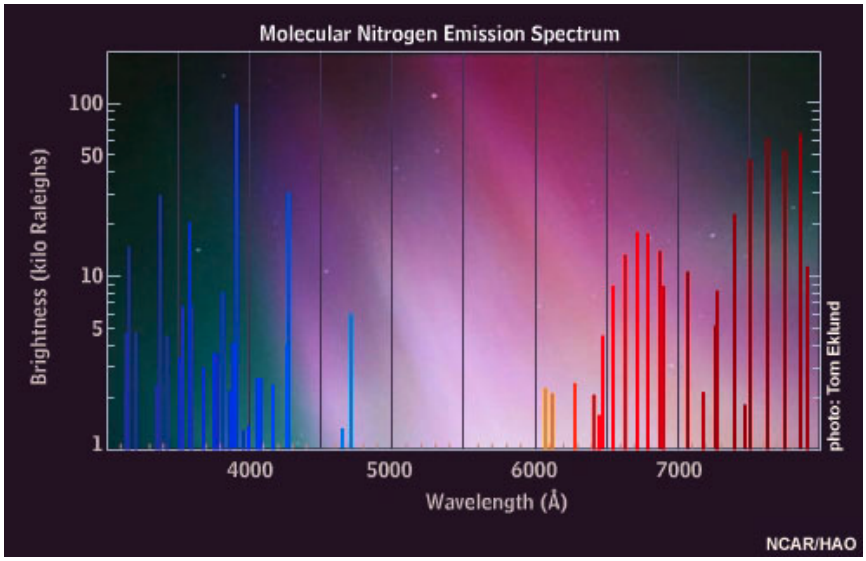

Figure 1-2: Spectral emission lines from Nitrogen [26]

emission can emit up to 1 GW of power at peak intensity, and possesses fine structural properties that appear in the 20-750 kHz frequency range [7].

One of the primary science questions for the AERO CubeSat mission is assessing the possibility of AKR penetration and propagation to low altitudes [7]. There have been simultaneous measurements made in space and on the ground, from the Geotail spacecraft and a ground-based array at South Pole Statio (SPS). SPS's location is magnetically connected to where AKR occur in the ionosphere. Due to the sharp cutoff of the ionosphere's plasma frequency, AKR emission should not be allowed to penetrate to the ground. However, Figure 1-3 shows an example of simultaneous measurements where AKR is visible from both space and ground perspectives. This leads to one of AERO's primary science questions: what propagation path did the AKR take that enabled it to penetrate the ionosphere and propagate down to lower altitudes? [7] Other RF targets of interest include Medium Frequency Bursts (1.6-4.4 MHz), cyclotron emission (2.8-3.0 MHz), and auroral hiss (up to 800 kHz) shown in Figure 1-4 [7]. Some of these types are very compact in frequency, such as cyclotron emission, while others possess more diffuse fine scale structures. While all originate from different types of physical processes, each tells us something fundamental about the energy exchange going on in the aurora, making them significant targets of in-

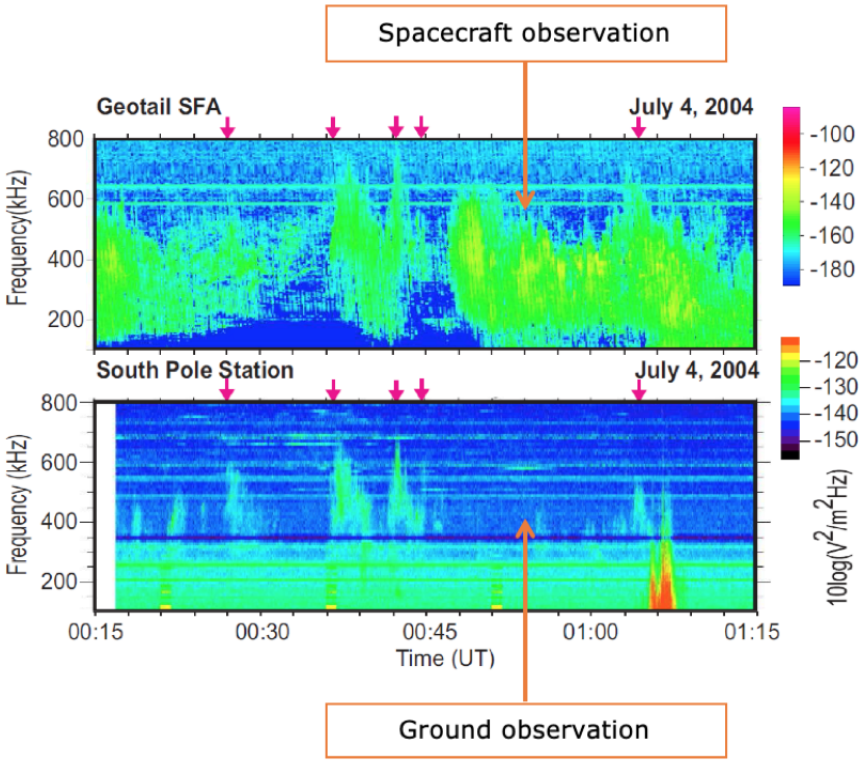

Figure 1-3: Ground and space based observations of Auroral Killometric Radiation [18]

terest. The AERO VS is sensitive enough to probe these diverse science targets to attempt to answer the many remaining questions about these auroral types.

Optically, the AERO ASP plans to measure both green-line and red-line emission, both types that are well-characterized and good targets for comparative measurements between the radio VS data products and optical sensor. Optical detection of these emission lines provides a binary (yes/no) response for confirming the presence of auroral emission.

1.2.3 Overview of Radiometry and Key Terms

Typically, a radiometric budget assumes incoherent sources; this is an appropriate assumption for the dynamic and complex nature of auroral emission [29]. Radiometry is defined as the measurement of light across any portion of the electromagnetic spectrum, with measurements described in terms of absolute of units of Watts m^{-2}

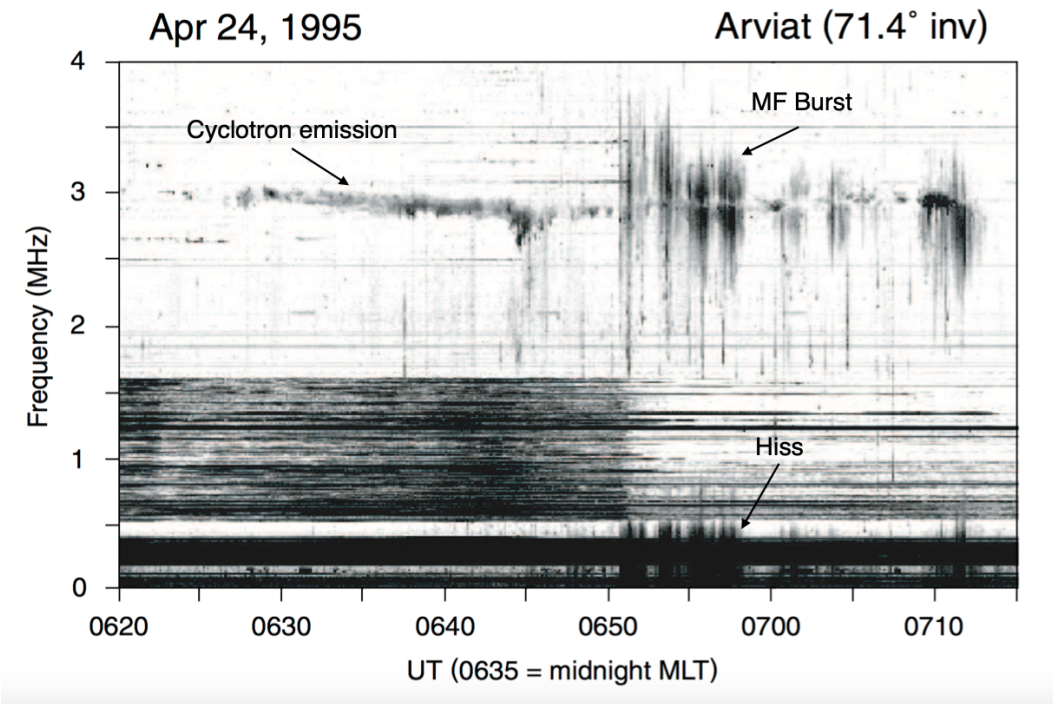

Figure 1-4: Ground-level spectrogram showing three types of auroral emission targets [17]

or photons sr^{-1} s^{-1} [2, 27]. It differs from photometry in that optical measurements for photometry are weighted to account for the sensitivity of the human eye. Photometric measurements are described in terms of illuminance or radiance in units of lumens m^{-2} (lux) or magnitudes [2, 27]. In this work, we use radiometry.

Units for measuring radiation are often confusing. We attempt to clearly define the terms and units that are used in this work. For radiometry, radiation intensity is described in terms of radiance or irradiance. Radiance represents intensity with quantum units of photons m^{-2} s^{-1} sr^{-1}. Irradiance is in terms of flux with units of photons m^{-2} s^{-1} [29]. Radiance is sometimes referred to as intensity and irradiance as emittance, with units of W m^{-2} sr^{-1} and W m^{-2} [29]. These terms can be spectrally dependent, when divided by source wavelength or wavelength range, with units of W m^{-2} sr^{-1} $\mu\mathrm{m}^{-1}$ and W m^{-2} $\mu\mathrm{m}^{-1}$. It should be noted that radiance differs from surface brightness in that the latter is a relative term that describes source intensity with considerations of distance between the detector and source [29].

For auroral sensing applications, photon flux is described in terms of Rayleigh, an atypical unit that is based on line emission in a column. The Rayleigh is applied in atmospheric radiometry when dealing with monochromatic radiation, such as the aurora, and is defined without photometric dependence on the color response of the human eye [3, 29]. The Rayleigh unit is described in further detail in Section 2.1.2.

1.2.4 Space-Based Optical Auroral Observations

This literature review focuses on existing efforts for space-based sensors performing auroral intensity detection. The objective for AERO's optical measurement is to sense auroral emission in multiple spectral bands, rather than image auroral events. With optical auroral detection as a secondary objective, there are no spatial resolution requirements for the ASP optical measurement. It should be noted that it is rare that an auroral targeting mission makes optical detection a secondary objective, and even more so that the detection is made with a simple photodiode, as is the case with AERO.

A typical suite of instruments for measuring optical intensities of aurora include cameras or other imaging devices such as Charge-Coupled Devices (CCDs) and Intensified Charge-Coupled Devices (ICCDs), photometers, spectrometers and interferometers. Trades on sensor spectral resolution, image swath size, and desired temporal resolution help in the instrument selection process [14]. For example, all-sky imagers see averaged aurora rather than small-scale structures [29]. Spectrometers collect spectral images of narrow regions of the sky, enabling them to image complex small-scale structures. However, spectrometers typically have low temporal resolution, making it difficult to identify source location [14].

Tronsden 1998 noted at the time that projects targeting auroral imaging were steadily moving toward use of space-based rather than ground-based imagers [29]. Ground-based observatories have fixed locations and therefore limited viewing areas, but have the benefit of providing continuous night-time imaging [23]. The trend toward space-based missions includes NASA's Time History of Events and Macroscale Interactions during Substorms (THEMIS), a mission with five identical probes that

uses a suite of instruments to observe physical processes that occur during auroral substorms [32]. The THEMIS probes each hosted several instruments, including a solid state telescope that measured particle distribution functions, though none of the instruments involved direct auroral imaging [30]. NASA's Imager for Magnetopause-to-Aurora Global Exploration (IMAGE) mission was another space-based mission that combined neutral atom, photon, and radio imaging techniques to generate large-scale, simultaneous measurements of multiple regions of the Earth's magnetosphere [10]. IMAGE hosted complex instruments including energetic neutral atom, extreme UV, and radio plasma imagers to take high resolution measurements of the aurora [10]. Despite the added cost and complexity, space-based instruments provide opportunities to image larger swaths of the auroral oval. However, the spatial and temporal resolution of small numbers of space-based instruments at near-auroral altitudes are typically less than that of ground-based, all-sky imagers [29].

CCDs and ICCDs have been the primary instruments of choice for auroral imaging. However, baselining more sophisticated instruments that require more SWaP was not reasonable approach for AERO's non-imaging optical auroral detection requirement. A simple, silicon photodiode array equipped with optical filters to differentiate between color channels was selected for AERO's ASP. The selected sensor is a Commercial Off the Shelf (COTS) part, and not space qualified. Based on a review during part selection, the author did not find any reports of the use of silicon photodiodes or arrays of photodiodes used for space-based auroral radiometry.

There have been a few CubeSats with auroral studies as their primary science objective. For example, the Radio Aurora Explorer (RAX) 1 and 2 CubeSat missions; RAX 1 was the first CubeSat commissioned by the National Science Foundation [6]. The RAX mission objective involved the assessment of plasma instabilities and field-aligned irregularities at altitudes from 80 - 400 km using a direct-conversion radar receiver operating from 426 - 510 MHz [6]. Though RAX also focused on aurora, RAX's science objectives and payload are substantially different from AERO. The ANDESITE mission will use nanosatellites to measure magnetic fields [8]. Future mission designs include concepts like the Earth X-ray Aurora CubeSat Telescope

(EXACT) to simultaneously observe Earth's X-ray aurora and magnetic field properties via an x-ray telescope coupled with magnetometers [4]. These example missions do not involve optical measurements of auroral emission.

1.2.5 Overview of Radiance Budget Technique

A high-level example of parameters included in a typical radiance budget for a passive optical sensor is shown in Figure 1-5. An overly simplified description of the approach involves mapping the auroral emission to spectral radiometric intensity at the sensor input and then to an output signal in terms of sensed photon count or radiance. Auroral input is typically in Rayleighs. This unit is further discussed in Chapter 2.

A typical approach for estimating a sensor's radiometric performance is presented in Space Mission Engineering: The New SMAD [31]. First, spacecraft orbital parameters are defined. Orbit parameters affect decisions regarding sensor viewing parameters, that in turn relate to the size of detector pixels as they are projected at the sensor's ground scene, an area that determines the power density per solid angle at the detector. Next, pixel properties and optical parameters affect the fraction of sensed radiation that will be detected as incident power at the sensor optic. Several factors relate to the measured incident power, including blackbody spectral radiance (for background, as auroral emissions are not blackbodies), integrated upwelling radiance, and the sensor's operational bandwidth. Additionally, propagating signals experience effects from the atmosphere that may refract away or significantly attenuate radiation along its path to the detector, captured in atmospheric transmission loss.

Once the signal propagates through the sensor's optic, it is further attenuated by optical transmission loss, a property inherent to the optical surfaces that are part of the sensor instrument. The sensor's ability to convert incident photons to photoelectron carriers that are then converted to a digital signal at the analog to digital converter, ADC, is the device's quantum efficiency. This parameter can also contribute to losses.

The goal is an assessment of the sensor's signal-to-noise (SNR) ratio. In this work,

SNR is the sensor's Minimum Detectable Signal above the noise floor as defined by the instrument's electronics. Once contributions from the aforementioned noise terms are applied, the SNR of the sensor may be calculated as a ratio of the number of available electrons to the total number of noise electrons in the system.

A notable example of auroral radiometric analysis, as opposed to the generic analysis in SMAD, is presented by Trondsen 1998 [29]. Trondsen uses a CCD, and considers terms such as electron multiplication noise, dark noise, and an intensifier noise factor [29]. For reference, some results from Trondsen's radiometric analysis for a CCD are shown in Table 1.1. Their resulting SNR versus column emission rate, or photon flux in R, for different imager types is shown in Figure 1-6. This thesis does not have same level of detail in treatment of the radiance analysis because of the limited information available for the COTS photodiode array.

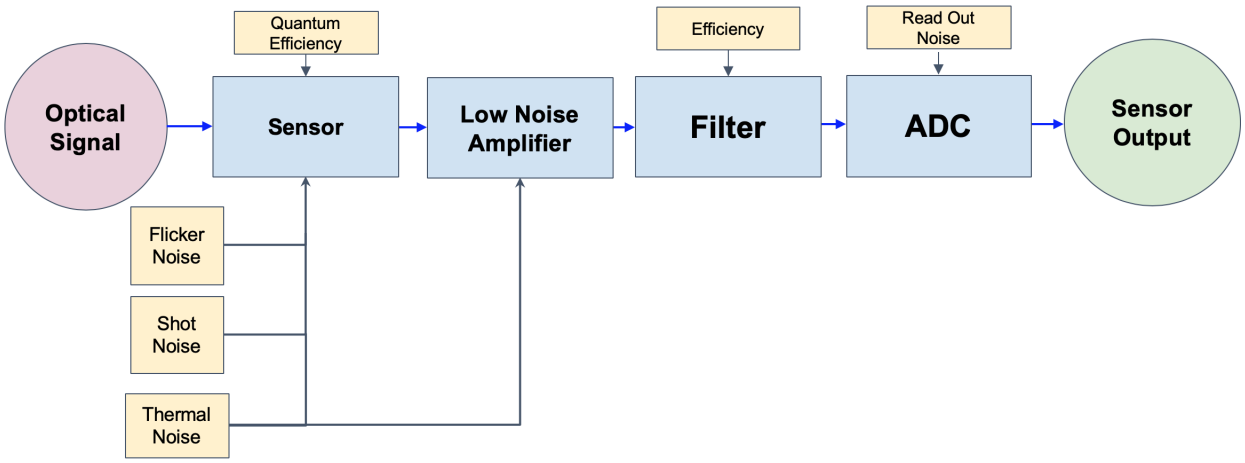

Figure 1-5: High-level overview of traditional radiometric analysis approach

1.3 The Auroral Emission Radio Observer (AERO)

The Auroral Emission Radio Observer (AERO) is a 6U ($10 \times 20 \times 30$ cm^3) CubeSat that will observe low-frequency (100 kHz - 15 MHz) properties of common auroral events such as Auroral Kilometric Radiation (AKR), auroral hiss, and Medium Frequency Burst (MFB). The spacecraft will operate in a near-polar, sun-synchronous

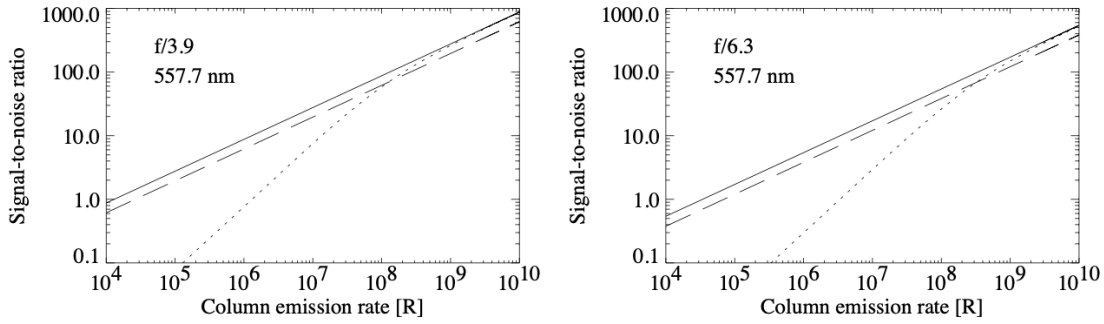

Figure 1-6: Calculated SNR vs Emission rate for CCD (dotted line), ICCD (dashed), and ideal detector. Results from Trondsen 1998 [29]

Table 1.1: Radiometric Results for CCD [29]

Parameter	Value	Unit
Photocathode QE	28	% (at 557.7 nm)
Photocathode Dark Current	0.1	nA m^{-2} (at 27° C)
CCD QE	67	% (at 557.7 nm)
CCD Dark Current	0.1	mA $m^{-}2$ (at 27°C)
CCD Read Noise	80	electrons
Image Integration Time	16.7	ms
Transmission, Nikon Lens	0.9	-
Transmission, Interference Filter	0.7	-
Threshold of Detection (pixel SNR)	2	dB

(noon-midnight) Low Earth orbit, supporting remote sensing of the auroral acceleration region in a near-Earth environment. AERO's primary payload involves a novel tape-spring, electromagnetic Vector Sensor (VS) antenna measuring 4-meters tip-to-tip once deployed from the CubeSat body. The VS forms electric dipoles and magnetic loops to measure the full electric and magnetic field vectors of radio signals at a common phase center [7, 21, 24, 16]. A more detailed discussion of the VS is provided in Section 1.3.2.

In addition to the science targets of interest discussed in Section 1.2.2, the mission's primary objective involves space-qualifying the VS, validating both the deployment mechanism as well as the fidelity of the sensor's resulting data products. To

validate the VS's measurement, AERO will first measure well-characterized cyclotron harmonic phenomena prior to sensing the other targets of interest such as the AKR [7]. Successful performance of the VS antenna will provide a high-performing technical solution via remote sensing techniques that serve to address some of the key knowledge gaps surrounding these emission types.

AERO will deploy alongside a second, identical spacecraft, the Vector Interferometry Space Technology using AERO (VISTA). Together, AERO-VISTA will enable a novel suite of space-based interferometric measurements, such as interferometric beamforming and imaging, using both VS antenna systems [21]. Successful completion of the AERO-VISTA CubeSat missions will provide valuable measurements for radio auroral emission of several types, and together they form the first space demonstration of vector sensor radio interferometry [21]. A space-based interferometry platform that operates at altitudes above the ionosphere will also enable future scientific studies that rely on operation at frequencies below the ionospheric plasma frequency, such as satellite constellations to observe solar system radio emissions, coronal mass ejections, and solar radio bursts [21, 16, 24].

1.3.1 Auxiliary Sensors Package (ASP)

The AERO-VISTA satellites include an Auxiliary Sensor Package (ASP) composed of Commercial-Off-The Shelf (COTS) components. These sensors augment the vector sensor measurements by providing supplemental optical and magnetic data, generating high-fidelity contextual information for the auroral events observed. Considering the ASP as a secondary payload allows us flexibility in sensor type selection, enabling use of smaller, cheaper, COTS components. Scientific objectives prioritize radio emission observations of the aurora, relaxing the constraints on optical emission observed with the ASP sensor suite. Though some performance requirements are relaxed, each component is required to have low-levels of Electromagnetic Interference (EMI) to protect the sensitivity of the VS from spacecraft induced noise in the science measurement band.

Optical measurements provide independent confirmation of events through green-

line and red-line auroral arc intensity observations. The ASP uses an AMS AG AS7262 single chip, six-channel visual band sensor as the selected optical detector [1]. This sensor is the primary focus of this work, and is referred to throughout as a spectral photometer. Its spectral bands enable observation of both green-line (557 nm) and red-line (630 nm) emission, and its operation is described in greater detail in Section 2.2. The ASP also includes four magnetometer chips to make in-situ magnetic field amplitude and vector direction measurements with a precision better than 100 nT. Magnetic data align the RF VS measurements and polarization with the local magnetic field direction and also help to localize RF measurements with respect to the auroral oval by observing Birkeland Region 1 and 2 field-aligned currents. The Birkeland region currents, shown in Figure 1-7 are a well-understood component of the auroral oval. Comparison of magnetometer data with the International Geomagnetic Reference Field (IGRF) models can enable location of these well-characterized regions to serve as a constant point of comparison for validating AERO's RF observations [21, 7]. The ASP also includes a Raspberry Pi camera equipped with a 195° FOV fisheye lens for both confirmation of VS deployment and to serve as a tool for troubleshooting issues that may arise on-orbit. The work presented in this thesis focuses on the AMS AS7262 sensor and how to assess its sensitivity for achieving AERO's mission objectives.

The individual components of the ASP are packaged into two separate 39 × 48 × 115 mm^3 modules currently named Port and Starboard. A single module is shown in Figures 1-9 and 1-11a, where each module contains two optical sensors, two magnetometers, one engineering camera, and a Raspberry Pi Zero that serves as the system's microprocessor. Each module includes three boards that host the individual components, as well as the appropriate inter-module connectors and those required for interfacing with the spacecraft bus (see Figure 1-8). Power, data and timing interfaces between the two ASP modules and spacecraft bus are defined in Figure 1-10.

Figure 1-12 shows both ASP modules integrated into the 6U CubeSat frame, one positioned on each side of the stowed VS payload. The optical sensors are positioned

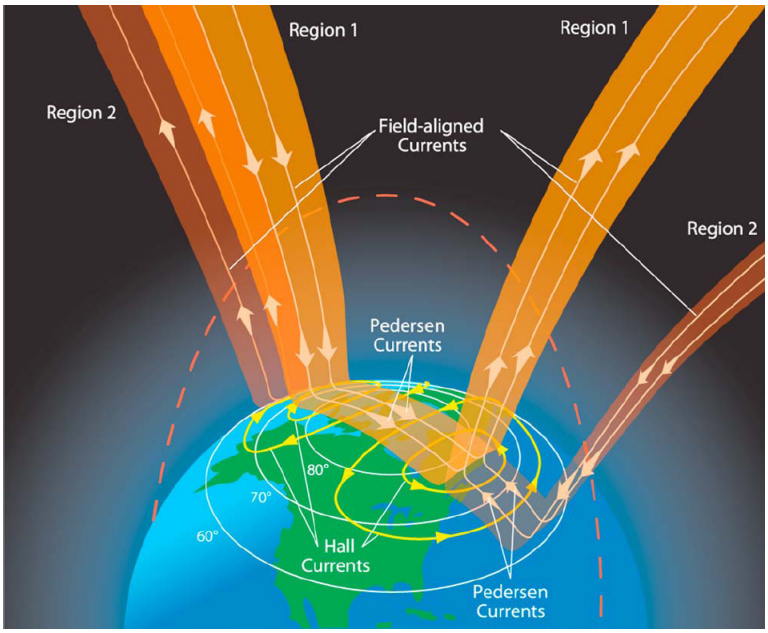

Figure 1-7: Birkeland Region 1 and 2 magnetic field-aligned current [19]

in the module packaging such that each views an independent face of the CubeSat body. This is done intentionally to allow for both redundancy in case of sensor failure, as well as sensor measurements that are independent of spacecraft orientation. The VS antenna is considered to be omnidirectional, meaning there are loose constraints on spacecraft orientation for the purposes of taking RF measurements.

1.3.2 Vector Sensor Antenna

The AERO CubeSat's primary payload is the novel Vector Sensor antenna. The VS consists of four 2-meter long dipole antennas that extend orthogonally from the spacecraft as shown in 1-13. Additionally, a 2-meter monopole extends vertically to complete the loop configuration, requiring a total of nine fiberglass composite tapes. The VS lives stowed in an approximately 2U (10 x 10 x 22 cm^3) volume within the CubeSat's structure prior to deployment initiated via a ground command. MIT Lincoln Laboratory designed a telescoping mechanism that allows the antenna to rigidly deploy from the CubeSat body free of obstruction from the solar panels. Once fully deployed, the tape-spring antennas form a total six orthogonal dipole and electrically small loop antennas allowing remote sensing measurements with increased

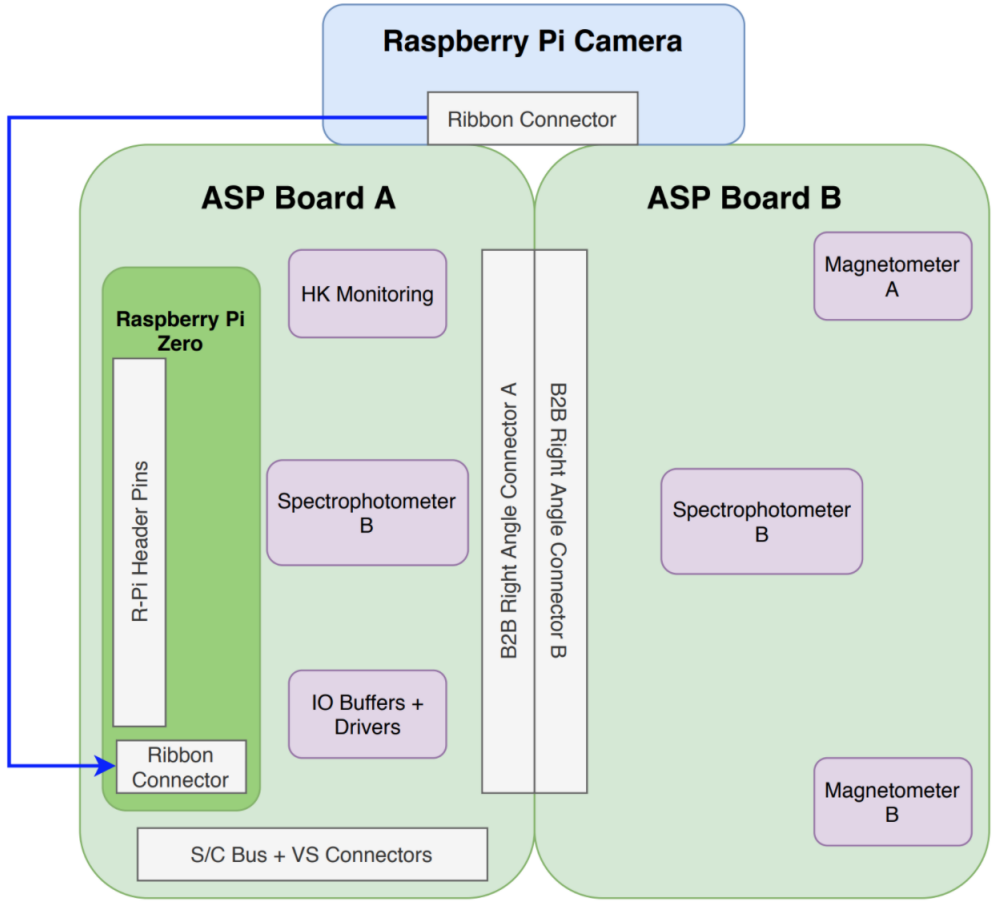

Figure 1-8: ASP Hardware block diagram

degrees of freedom compared with other antenna systems [21].

Antennas with fewer degrees of freedom are limited to partial scalar Electric (E) and magnetic (H) field measurements. The VS geometry allows the instrument to sample both amplitude and phase at a single point in space with a common phase center of both field vectors [21, 24]. This complex instrument enables concurrent measurements of time and angle of arrival, as well as polarization information of each observed event. In conjunction, these simultaneous measurements provide insight to source intensity and relationship of signals as they arrive at each antenna element [21]. Emergent data products of measuring full E and H fields include emission polarization type, as well as the resulting Poynting vector of the electromagnetic wave, indicating the wave's direction of propagation [21, 24].

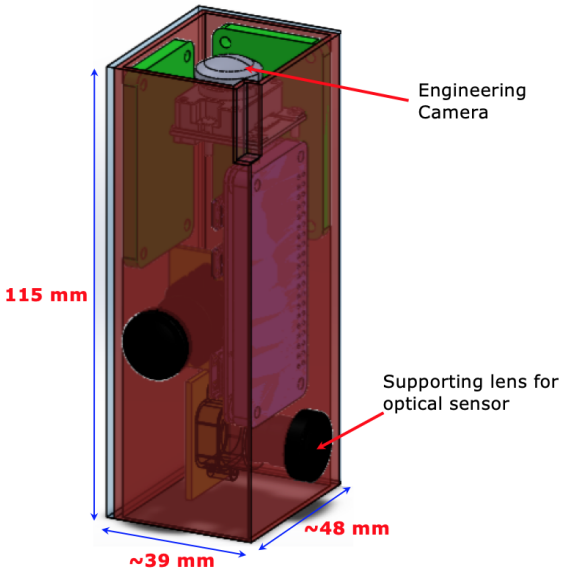

Figure 1-9: Isometric view of single ASP module

1.3.3 Vector Interferometry Space Technology Using AERO

The Vector Interferometry Space Technology Using AERO (VISTA) CubeSat is a carbon-copy of AERO that serves as a complementary companion. Both AERO and VISTA host identical vector sensing antenna systems. Combined measurements from the AERO-VISTA spacecraft system will demonstrate Vector Sensor interferometric imaging, beam forming and nulling. Having an operational twin to AERO is advantageous from a redundancy perspective. Should one CubeSat fail, the other provides an opportunity for the mission to still accomplish some of its science objectives.

A primary objective of the combined missions is to prove the sensor's ability to maintain desired measurement sensitivity, even in the case of injected terrestrial interference in the science band of interest [21, 24]. Traditional requirements for space-based, low-frequency interferometric sensors result in orbits further away from Earth and its interference (e.g., a geosynchronous or even lunar orbit) for sensitivity reasons [21]. Large constellations would normally be required to achieve the desired sensitivity, resolution, and number of measurements. If successful, VISTA's technology demonstration has the potential to scale back future mission architectures by

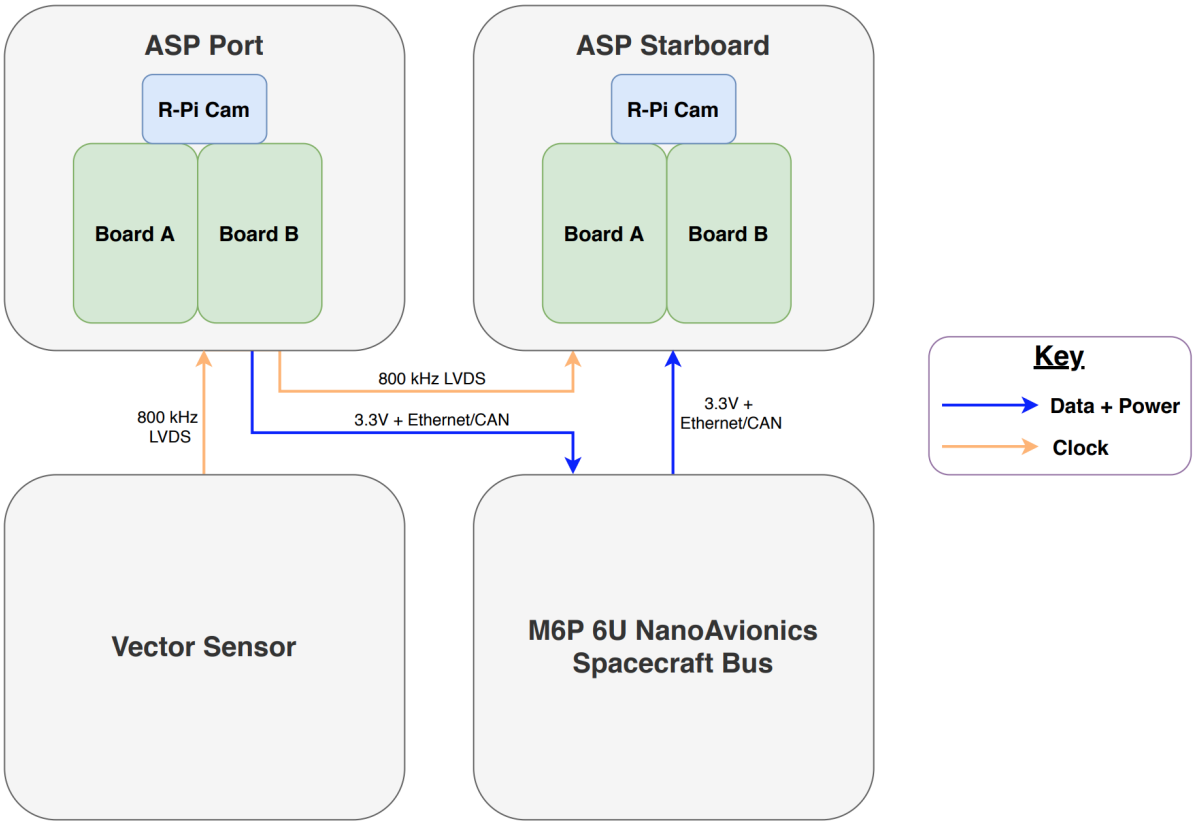

Figure 1-10: Block diagram of external ASP module connections

enabling low-frequency VSI measurements in LEO, where terrestrial noise is high. [21]

1.4 Thesis Objectives and Organization

The objective of this thesis involves proving the feasibility of using a COTS spectral photometer to provide contextual measurements that confirm auroral events. This work seeks to answer the questions: 'Does the sensitivity of the selected sensor suffice for auroral arc detection?' and 'What would the signal from an auroral arc look like in each of the bands as we fly overhead in LEO?'

The purpose of the ASP and optical sensor is to independently confirm AERO's RF VS measurements. This work considers multi-band measurements of the aurora and develops a payload configuration and tools to assess the COTS sensor's perfor-

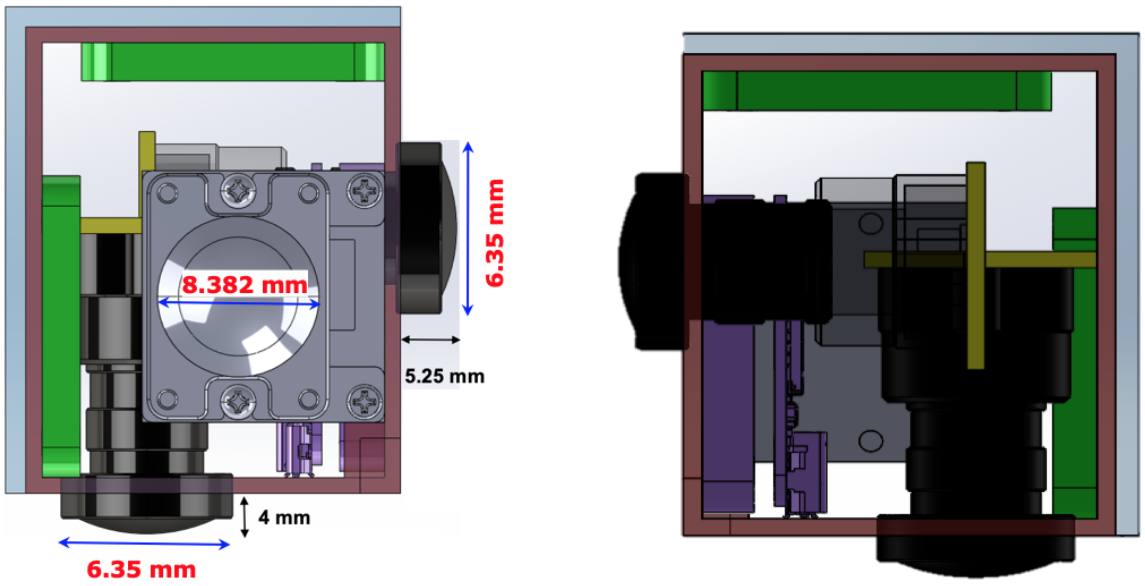

(a) Top View of ASP CAD assembly with labeled aperture diameters

(b) Bottom view of ASP CAD assembly showing 2 orthogonally mounted AS7262 sensors

Figure 1-11: Top and bottom views of single ASP module

mance in making auroral observations. The main focus of this thesis is a radiometric sensitivity analysis to determine the type and intensities of auroral events observable by the selected sensor. Results from this work will drive mission design decisions for AERO regarding the type of optical sensor selected for the ASP, placement within the spacecraft bus, sensor quantity, and any supporting optics to interface with the sensor aperture. Overall, the tools and analysis in this help to validate relevant Level 1 and Level 2 requirements for both the AERO CubeSat mission.

This thesis develops a radiometric approach for verifying an optical sensor's ability to provide the AERO VS with independent confirmation of visible auroral events. Chapter 1 provides an introduction to the AERO CubeSat mission, auroral radiometry terms, and the role of the Auxiliary Sensor Package. Chapter 2 provides a detailed discussion of the AMS AG AS7262 COTS spectral photometer, and provides context for the measurement type and geometry. Chapter 3 describes the analysis and methodology. Chapter 4 discusses analysis results. Lastly, Chapter 5 provides an overview of future work, including proposed experimental setups for validating the

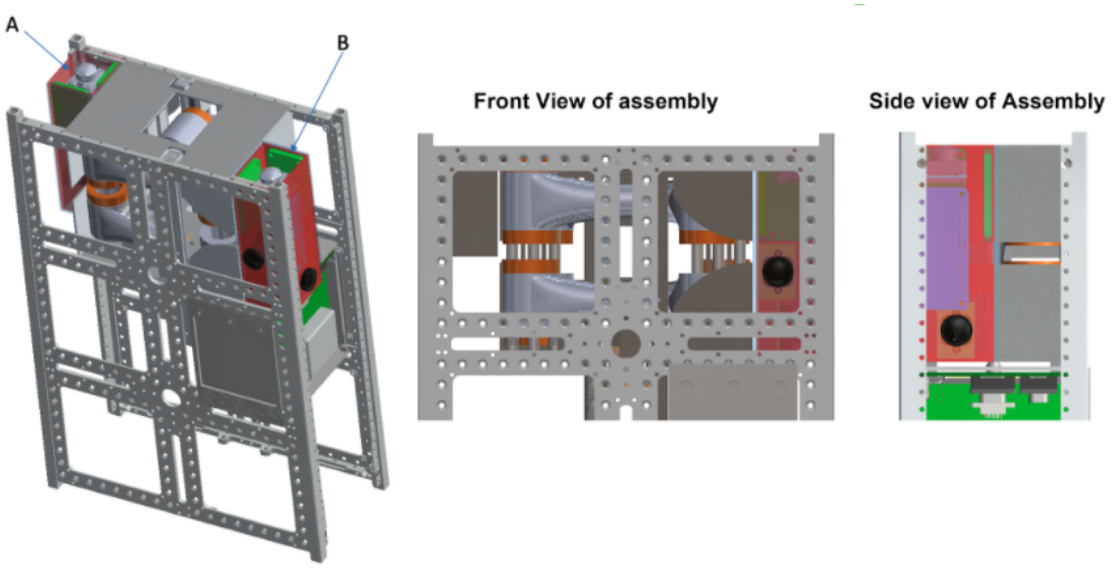

Figure 1-12: Both ASP modules integrated into 6U CubeSat frame (credit Mark Silver at MIT Lincoln Laboratory)

sensor's performance in a laboratory environment.

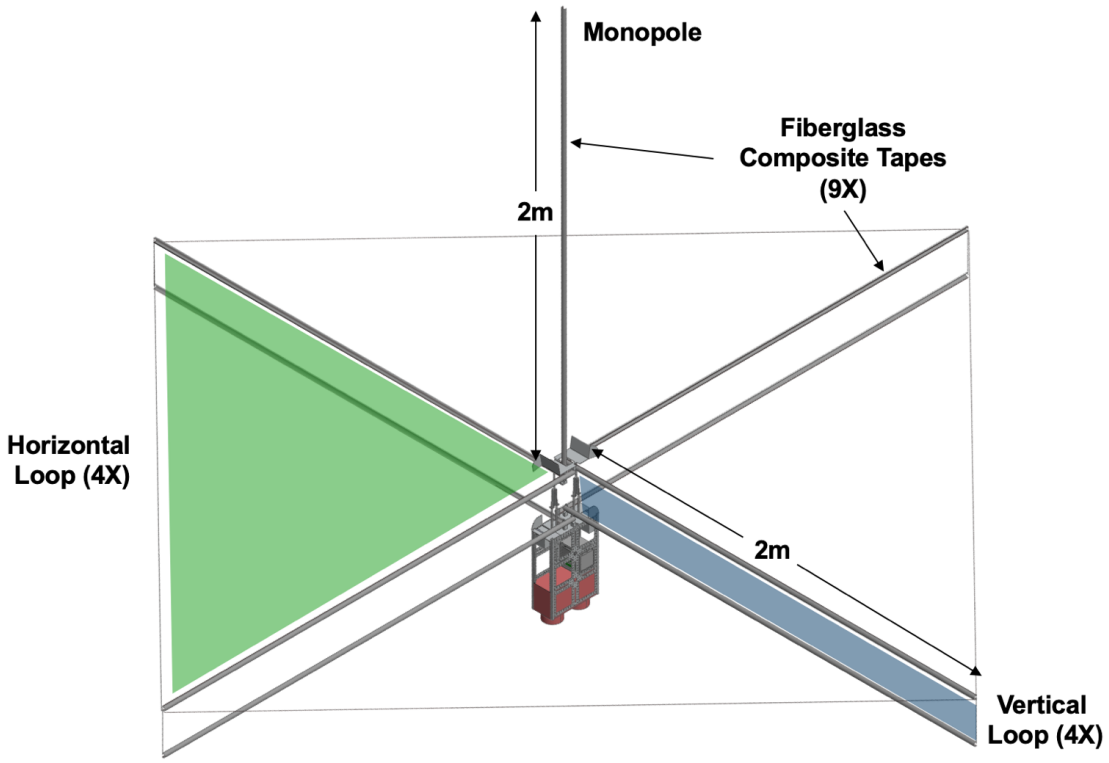

Figure 1-13: CAD of full extended VS antenna from 6U CubeSat body (credit Mark Silver at MIT Lincoln Laboratory)

THIS PAGE INTENTIONALLY LEFT BLANK

Chapter 2

Approach

2.1 Physical Principles of Measurement

Key sensor targets are green (557.7 nm) and red (630 nm) line emission. The sensor should be able to differentiate between measurements that contain auroral line intensity and those with just background emission or terrestrial interference from the Earth.

Due to the physics of aurora generation, source emission is observed as spectral, or alternatively molecular/atomic, line emission. Green-line and red-line auroral spectra are narrow-band due to their specific atomic interactions and energy level transitions. It is not appropriate to treat aurora as a blackbody source. However, spectral sensors may have channel bandwidths that are significantly wider than the auroral lines. A radiometric budget for the sensor should include treatment of any background signal, including blackbody radiation from Earth, that the sensor picks up in its band that contains the auroral emission line. This work focuses on the ability of the sensor to detect auroral emission, and in future work will include sources of background radiation and interference that may affect measurements. Further discussion on this is found in Chapter 3.

2.1.1 Auroral Source

Auroral emissions also exist outside of the visible bands of the AERO sensor, but this work considers those that are within the bands of the AS7262 sensor. Table 2.1 is an adaptation from Trondsen 1998 that shows electron auroral species with wavelengths within the sensitivity range of the sensor [29]. All listed intensity values are relative to O^1S International Brightness Coefficient (IBC) III aurora at 557.7 nm with an intensity of 100 kR [29, 5, 13]. Minimum and maximum ranges of the auroral species are listed. Some emitters are spectrally distributed in wavelength as the result of effects such as Doppler shifts and pressure broadening. Table 2.5 shows that the maximum sensible wavelength is 690 nm on the red channel. Emissions from $N_2 1P$ and $N_2^+ M$ are likely out of the sensor's range. The minimum sensible wavelength is 410 nm on the violet channel. Emissions from $N_2^+ 1N$ are likely also out of range.

Table 2.1: Auroral emitters within sensitivity range of AS7262 sensor [29]

Emitter	Wavelength (Angstrom)	Wavelength (nm)	Rel Intensity (kR)
$N_2^+ 1N$ (Min)	3910	391	150
$N_2^+ 1N$ (Max)	5220	520	150
$O_2^+ 1N$ (Min)	5270	527	26
$O_2^+ 1N$ (Max)	6820	682	26
O^1S	5577	557.7	100
$N_2 1P$ (Min)	5960	596	880
$N_2 1P$ (Max)	18870	1887	880
$N_2^+ M$ (Min)	6120	612	630
$N_2^+ M$ (Max)	15850	1585	630
O^1D	6300	630	2-100

Table 2.2 provides a reference for typical photon flux values in Rayleigh alongside their corresponding radiometric values as defined by the IBC [28]. Listed radiance values are relative to green-line emission at 557.7 nm. IBC levels III and IV represent intense visual events, with relative brightness levels synonymous to a moonlit cumulus and full moonlight illuminated skies respectively [28]. IBC II levels are only slightly above the sensitivity threshold of the human eye and are therefore only visible in dark

sky conditions [28].

Table 2.2: IBC Levels in Rayleigh with radiometric conversions [28]

IBC Level	Rayleigh	Radiance
I	1 kR	2.833x10^{-7} W/(m^{2}sr)
II	10 kR	2.833x10^{-6} W/(m^{2}sr)
III	100 kR	2.833x10^{-5} W/(m^{2}sr)
IV	1000 kR	2.833x10^{-4} W/(m^{2}sr)

2.1.2 Definition of the Rayleigh Unit

All auroral photon flux levels in this thesis are presented in units of Rayleigh. In this section we provide context for the Rayleigh and its relation to source radiance. The Rayleigh unit is named in honor of Lord Rayleigh, who in 1930 achieved the first successful measurement of absolute intensity of nighttime auroral airglow [3, 12]. The unit is defined such that it represents derivation from both observation and the physical process of auroral generation [12].

The Rayleigh unit describes source radiance with respect to photon emission rate per unit of surface area rationalized by some solid angle set by the detector [3]. The unit is originally defined in terms of angular surface brightness, B, generally expressed in terms of 10^6 quanta cm^2 sec^{-1} str^{-1} [12]. Source emission rate is useful for describing auroral emission, where the angular surface brightness is distributed over a column infinitely extended away from the sensor. This column has a cross-sectional area of one cm^2 [12]. One Rayleigh = 10^6 quanta cm^2 column^{-1} sec^{-1}. The Rayleigh is frequently written in terms of photons rather than quanta, though both expressions are identical. The term 'column' is used to indicate that the Rayleigh encompasses auroral source emission rate in the form of a column with an undefined length. Note that the Rayleigh unit is a generalization that does not compensate for self-absorption or non-isotropic auroral emission, meaning that it describes an apparent emission rate rather than an absolute measurement [12, 29].

The Rayleigh describes the rate at which photons emitted from auroral airglow emission strike a surface with a normalized area of one cm^2 [3]. It can be related to source intensity through the following relation [3]:

$$I = 4\pi 10^{-10} L \quad [R] \tag{2.1}$$

where I represents source intensity in units of Rayleigh, and L is source radiance in photons s^{-1} m^{-2} sr^{-1}. Rearranging the terms as shown in Equation 2.1 provides source radiance in quantum units, a form more appropriate for the radiometric analysis presented in this work. In this work, we assume that Rayleigh values used encompass all auroral radiation from one particular emission line. More details can be found in Section 3.2.

$$L = \frac{I}{4\pi 10^{-10}} \quad [\text{photons m}^{-2}\text{s}^{-1}\text{sr}^{-1}] \tag{2.2}$$

2.1.3 Measurement Geometry

Figure 2-1 shows the AERO spacecraft's geometry relative to the extended radiometric source as viewed by the spectral photometer. Table 2.3 outlines some of the key parameters that describe the sensor viewing geometry. We imagine a cone projected from the sensor's supporting optic away from the spacecraft until it intersects with the extended auroral source. Assuming spherical distribution of auroral radiation, the point of intersection of the sensor's projected view with the aurora makes the diameter of a circular 'ground scene' located at 100 km altitude above the Earth, approximately the location of the auroral F-region. The diameter of this ground scene determines the size of auroral event, or arc, the sensor can detect in a single instance. We note that auroral events may be spatially narrow, and may not fill the scene, as is assumed here. Adjusting the spacecraft altitude scales the ground scene, shown by Equation 2.3:

$$S_A = \pi\Big(\delta\ tan(\theta)\Big)^2 \quad [\text{m}^2] \tag{2.3}$$

where θ is half of the FOV of the instrument, as shown in Figure 2-1 and δ is the distance to the auroral event.

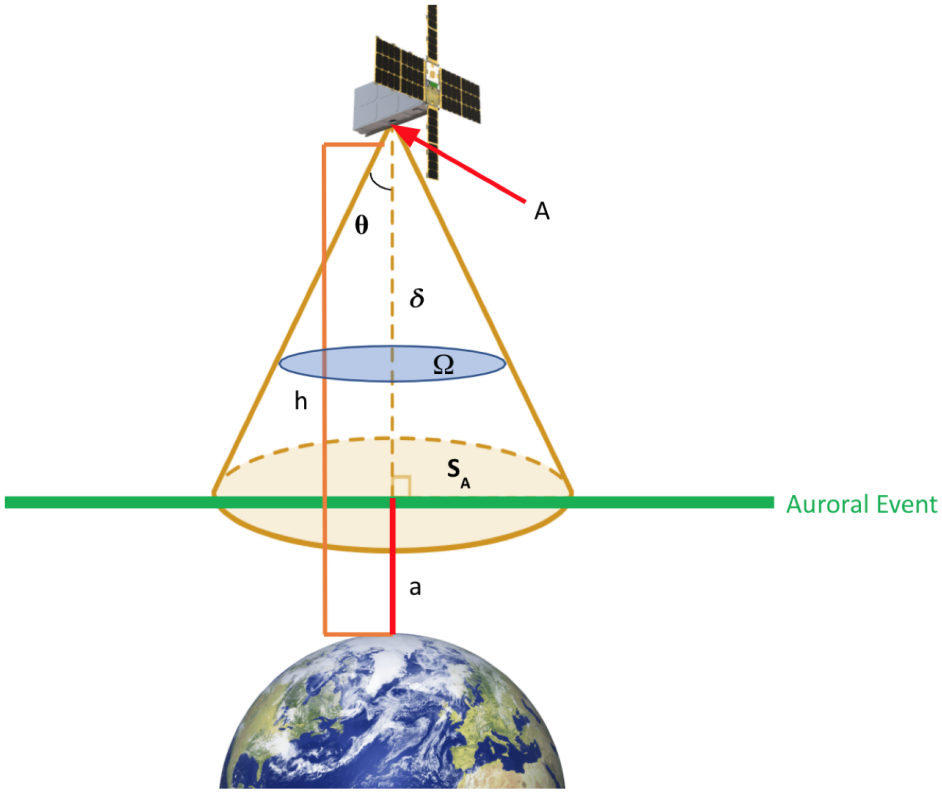

Figure 2-1: The geometry of the AERO spacecraft during data acquisition mode.

2.1.4 Derivation of Design Requirements

There are two key requirements, L1-11 and L2P-13, that drive the required performance of the AS7262 sensor. The requirements state that the spacecraft shall be capable of collecting measurements of visual band intensity of the aurora from the nadir direction at a minimum of two spectral bands [15]. This requirement stems from the desire for optical observations to place radio observations from the VS in the context of green-line and red-line auroral arc systems. It is necessary to include the ASP to satisfy this requirement. The requirement is written so that it is clear that it does not call for an image of the aurora, but rather proof that an auroral event exists during time of measurement. This relaxes the complexity and spatial resolu-

Table 2.3: Spacecraft geometry parameters

Parameter Name	Symbol	Value
Area of Lens	A	0.79 cm^2
Area of Ground Scene at Aurora	S_a	2.95 x 10^9 m^2
Spacecraft Altitude	h	450 km
Auroral Altitude	a	100 km
Distance between Sensor Aperture an Aurora	δ	350 km
Half Angle	θ	10°
FOV	Ω	20°

tion required of the selected sensor, allowing use of a simple, COTS photodiode array for the ASP. The selected six-channel spectral photometer satisfies the requirement for observations in at least two spectral bands by having six available. Note that the optical sensor will not be able to detect the aurora during daytime passes due to stray light from the sun. While the VS may observe day-side auroral events, there is no requirement for optical data to accompany these measurements.

When determining a sensor's sensitivity, a primary parameter of interest is the sensor's minimum detectable signal, *i.e.*, the sensor's Minimum Detectable Signal (MDS) for a given integration time [29]. The smaller the threshold of detection, the more sensitive the detector is to source emission. The requirements also state that the payload shall include sensor(s) capable of measuring night-time (spacecraft in umbra) intensity of the aurora at the $5{\times}10^3$ Rayleigh (1-σ) signal level in two spectral bands during vector sensor data collection [15]. This requirement constrains the MDS for the chosen sensor; the spectral photometer's performance must enable it to detect an auroral photon flux of at least 5 kR, meaning that a signal of this strength needs to appear above the sensor's noise floor.

Note that the aurora are temporally and spatially variable and have many different structural types. Writing a requirement on the sensor to detect a signal source of some desired intensity can be challenging. L2P-13 implies that the spectral photometer detects a 5 kR auroral signal in either the red-line *or* green-line band, or both if

both spectral lines are present in a single measurement. The required 5 kR signal represents the integrated flux from the auroral source at the green (557 nm) or red (630 nm) spectral lines.

For simplicity, we are not requiring use of the aurora's spectral response with a specific line shape at this time. When necessary, we model the spectral shape of both the green and red auroral line emission as rectangular functions, each assigned a conservative width of 10 nm. It is understood that these spectral lines are very narrow compared to the broader response of the spectral photometer's channel (bandwidth ±40 nm. Using this 'boxcar' approximation of the spectra is a simplification that allows us to model the 'brightest' green and red emission lines as well as, in future models, any incoming background radiation or interference within the wider sensor channel bandwidth.

Running the radiometric analysis with the proper shape of the auroral spectra and including sources of interference or background is beyond the scope of this work and is left as a future task. We interpret the requirement to mean that the sensor has the ability to at least detect a 5 kR auroral signature, assuming an emission line width of 10 nm or less, in either of the green or red bands. Figure 2-2 shows how the spectral bands fall on the sensor's channels with respect to each channel's normalized spectral responsivity. The radiometric analysis presented in this work serves as the first step in determining the sensor's ability to satisfy the mission requirements.

2.2 The AMS AS7262 Visible Sensor

The AG AMS AS7262 sensor is an array of six visual-band silicon photodiodes as shown in Figure 2-3. Each element is coupled with a unique spectral filter that uses nano-optic deposited interference filter technology to integrate Gaussian filters into CMOS silicon [1]. This narrows each photodiode's measurement band to create 6 visual channels over approximately 430 nm to 670 nm. Each channel has a full-width half-max (FWHM) of ± 40 nm. Spectral ID analysis is used to verify color sensed on each element. Given the sensor architecture, the instrument is referred to in this

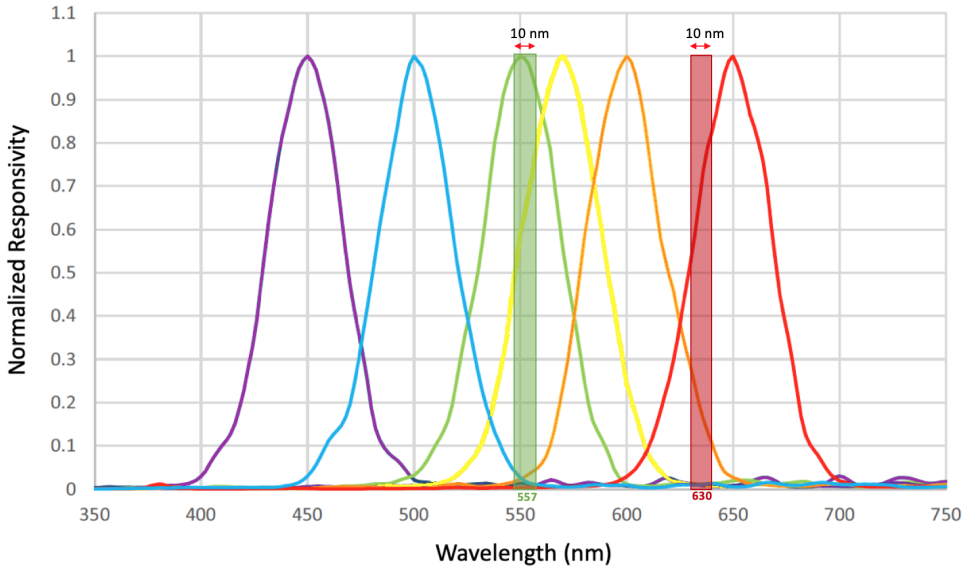

Figure 2-2: The 10-nm wide green-line and red-line auroral spectral bands overlaid on the AS7262's normalized channel responsivity [1]

work as a spectral photometer. The filters are robust in design and are reported to maintain stability over time and under variable temperatures. Table 2.5 shows the measurement bands of each channel, Figure 2-4 shows the sensor as it is currently configured, embedded on a development board, and Table 2.4 provides an overview of sensor parameters.

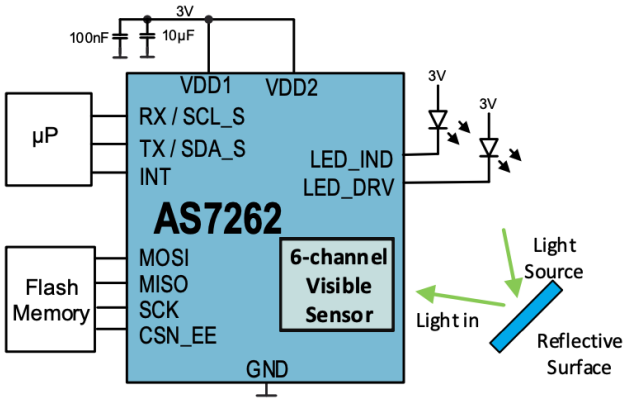

(a) AS7262 Sensor Block Diagram

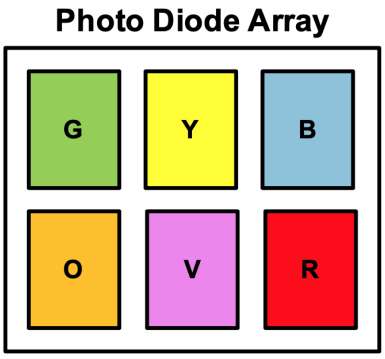

(b) The 6 Photodiodes in the AS7262 Sensor Array

Figure 2-3: Sensor Block diagrams from the manufacturer's datasheet. [1]

Silicon photodiodes are P-N junctions that generate electron-hole pairs via the

Table 2.4: AS7262 sensor parameters

Sensor Parameter	Value
Package Dimensions	4.5 mm × 4.7 mm × 2.5 mm
Package FOV	±20.0°
Supply Voltage	-0.3 to 5 V
Operating Current	5 mA
Operating Temperature	-40 - 85°C
Storage Temperature	-40 - 85°C
Clock Frequency	16 MHz
Wavelength Accuracy	±5 nm
Dark Channel Counts	5 counts

photoelectric effect. This occurs as a result of the material interacting with photons of sufficient energy to generate photoelectrons. The minimum detectable energy threshold in the case of this sensor is the amount of photon energy required to create a single count at the sensor's output. Detailed information about the sensor, such as device quantum efficiency, is not provided on the manufacturer's datasheet. We attempt to estimate the sensor's ability to convert incident photons to counts from the limited information that is provided on the datasheet. We use the vendor's measured value of counts on each sensor channel for a reference source; there is also limited information about the reference source and its configuration. We also use the Planck equation which gives the energy of a photon at certain wavelength. Our method does not provide any more detail on the sensor's quantum efficiency, but helps to understand whether aurora will register as one or more counts on the detector. See Section 3.2.3 for more detail.

The ASP sensor will not provide high-resolution optical data from the aurora, rather a simple measurement of counts from detected auroral presence in each of six visible bands. The sensor was chosen as the optical component of the ASP because of its simplicity, ease of integration, compact size, low-voltage operation, and low cost. The device was specifically chosen over a more sophisticated binary emission detec-

tion mechanism, such as a single broad-band photodiode, due to its multi-channel architecture. The spectral photometer is sensitive to both green and red light independently, a useful property that allows multiple opportunities for auroral detection. For example, if the sensor output shows increased counts on either the green or red channels compared with the remaining channels, we can confidently say an auroral event was detected over background terrestrial noise. It is unlikely that another source on-orbit will illuminate both green and red channels without showing strong signatures on the remaining four. A binary reading would provide information on the presence of emission, but would be unable to differentiate between detection of white light (or any other type of interference) and light from the aurora.

The sensor can be configured with either a UART or I^2C digital interface. It is currently configured to communicate with a PC via a USB-MPSSE cable that allows it to store raw and normalized counts, gain setting, and integration time in a CSV file. Future efforts in software development will reconfigure the data output to a packet format appropriate for inclusion in spacecraft health and telemetry data.

The sensor is not space-qualified and therefore requires laboratory testing to assess its performance in the space environment. This is discussed in more detail in Chapter 5.

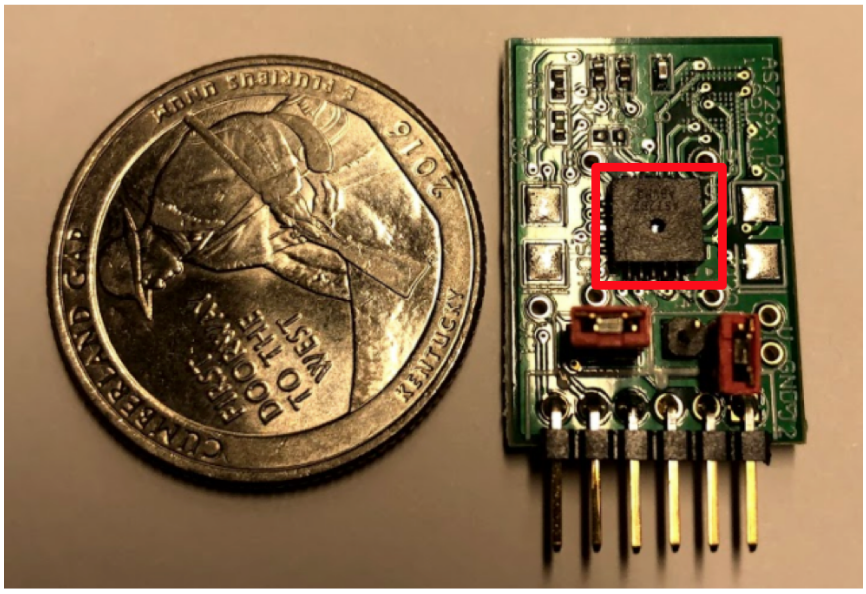

Figure 2-4: The AMS AS7262 Sensor embedded on a development board.

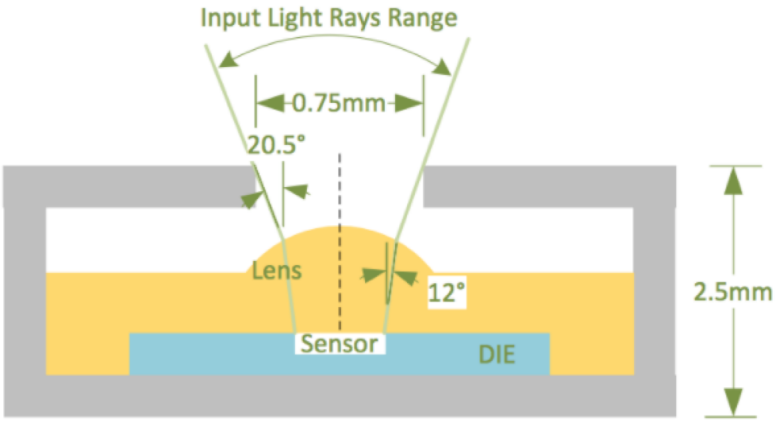

Figure 2-5: The AMS AS7262 sensor packaging with FOV. [1]

2.2.1 Description of Data Conversion

Each AS7262 device has two photodiode banks that allow the sensor to perform spectral conversion. The sensor has configurable bank modes of operation that select which data is integrated from the available registers corresponding to the six individual photodiodes. We will use BANK Mode 2, enabling the sensor to pull data from all six photodiodes for the same spectral conversion cycle as shown in Figure 2-6. To ensure that data in all registers comes from a single observed event, we need to support the minimum required Integration Time (IT) for a single bank conversion, which is 2.8 ms; therefore, the minimum required IT for fully converting both banks is 5.6 ms.

2.2.2 Supporting Optics

Each sensor will have a supporting 1-cm M12 (see Figure 2-7a) lens embedded in a cutout and mount located in the spacecraft chassis wall. Board mounts will be used to support lens alignment with the spectral photometer aperture. Table 4.11 shows the lens's physical parameters. The supporting optic serves to increase the sensor aperture, as the aperture embedded in the AS7262 packaging is only 0.75 mm. Radiometric analysis shows that an aperture of this size, perhaps unsurprisingly, will not meet the auroral detection requirements. The additional lens increases the photon

Table 2.5: Full bandwidth of the 6 spectral channels of the photodiode sensor.

Sensor Channel	Peak (nm)	Bandwidth (nm)	Min Channel Range	Max Channel Range
Violet	450	40	410	490
Blue	500	40	460	540
Green	550	40	510	590
Yellow	570	40	530	610
Orange	600	40	560	640
Red	650	40	610	690
		Full Range	**410**	**690**

collection capability. The spectral photometer's built-in aperture has a package-limited FOV of ± 20° as shown in Figure 2-5. It is desired that the support optic maintain a 20° full-cone FOV to better localize independent auroral arcs with respect to our spacecraft's orientation. A narrower FOV allows for easier differentiation between auroral structures.

Table 2.6: Physical parameters of M12 PT-021290 lens [20]

Parameter	Value
Part ID	PT-012290
Focal Length	2.1 mm
Iris	F2.2
Mount	M12x0.5
Image Sensor Size	1/3"

2.3 High-Level Analysis Approach

Figure 2-8 shows a high-level overview of the radiometric analysis approach. This model is different from standard approaches, like that outlined in The New SMAD

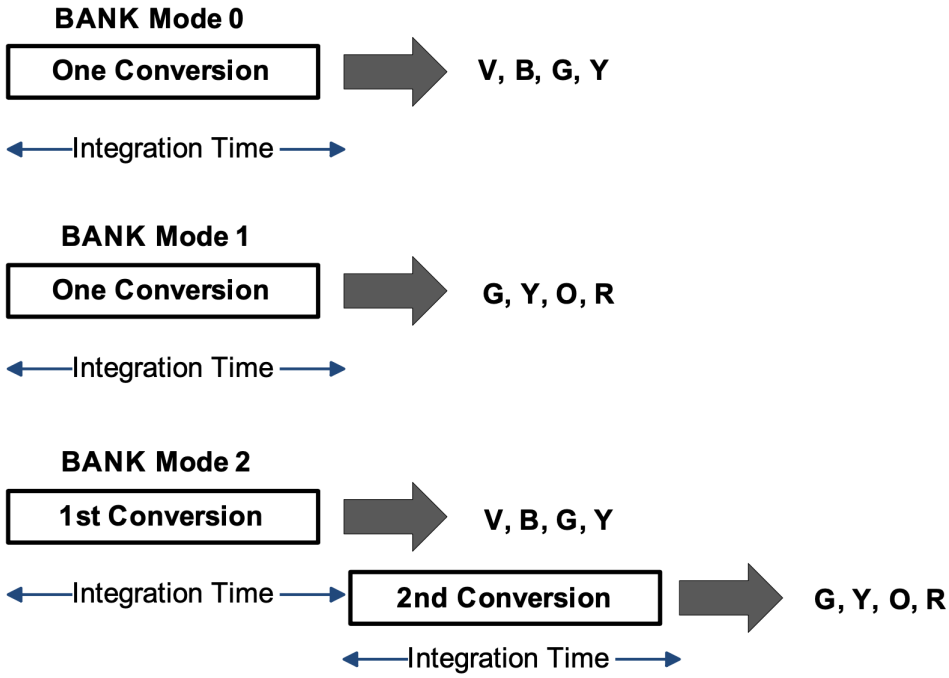

Figure 2-6: Sensor Bank Modes for Data Conversion [1]

[31], as this model is tailored to assess the performance of the AS7262 spectral photometer as it senses auroral emission across each spectral band. Model results allow evaluation of the sensor's ability to measure target auroral events (red-line and green-line emission) and assesses the sensor's ability to differentiate between auroral signatures and different sources of noise. The raw meaasurement is the total number of resulting counts. We consider a number of different test scenarios. The model methodology is discussed in detail in Chapter 3. We have developed a suite of planned laboratory tests to validate the radiometric analysis. More detail on these validation tests is summarized in Chapter 5. Unfortunately, due to the impact of COVID-19, we are unable to complete several of the desired tests at the time of writing.

2.3.1 Software Tools

Several different software tools were used in the development of the ASP and the radiometric assessment. The sensitivity analysis was originally developed in a shared

(a) Support lens for optical sensor

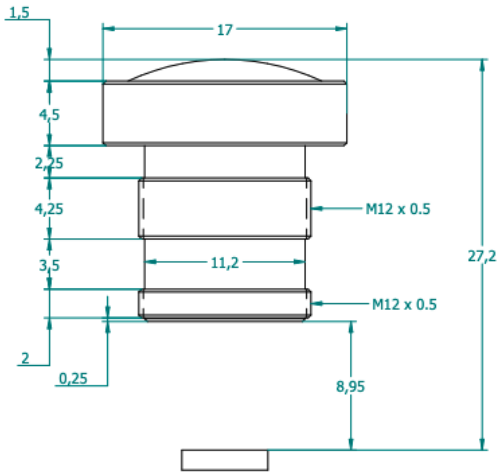

(b) Drawing of the supporting lens [20]

Figure 2-7: The supporting optic selected for expanding the collection area of the AS7262 spectrophotometer.

spreadsheet. It was then transferred to MathWorks' MATLAB to run the analysis cases. The ASP CAD for placing sensors in the module packaging was developed using Solidworks. The manufacturer of the sensor, AMS, developed a spectral sensing iSPI GUI for the AS7262 sensor that is used to set sensor parameters such as integration time and gain, as well as command the sensor to take data.

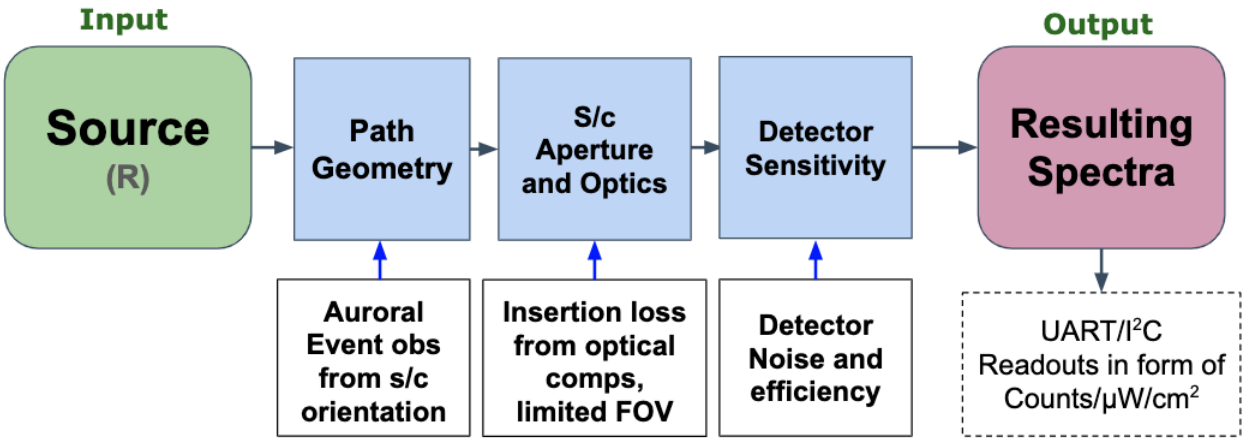

Figure 2-8: High-level block diagram of analysis approach.

THIS PAGE INTENTIONALLY LEFT BLANK

Chapter 3

Radiometric Analysis

3.1 Analysis Objectives

This radiometric analysis is a detailed mathematical model of the AS7262 sensor's expected performance on-orbit. The analysis objective is to compare the resulting threshold of detection for a single sensor as a function of multiple parameters such as spacecraft geometry, sensor counting efficiency, and intensity of the observed auroral phenomena. Parameters considered for each test case are shown in Table 4.1 in Section 4.1. The output of the AS7262 sensor is in units of counts. Results are presented in terms of marginal counts where the minimum requirement is one. We do not yet have enough data about the noise properties of the detector, such as readout noise and understanding of the different gain settings used to capture dark counts and calibration source counts to calculate meaningful SNR values. However, we do have enough information to determine whether or not auroral input signals will be strong enough to achieve a count of 1 on the detector. If the input cannot achieve a count of 1, we will not be able to detect the signal. We will still present the approach to SNR calculation, so that it can be calculated once we have enough information about the detector noise properties.

This model serves as the first step in the verification and validation process to confirm if the sensor's performance can meet the system requirements outlined in Section 2.2.1. Requirement L2P-11 specifies the minimum detection threshold of

auroral intensity as 5 kR. This is the lowest intensity signal the sensor must detect to provide useful supplementary optical data. Results presented in Chapter 4 show the sensor's performance in terms of resulting signal margin above the sensor's noise floor for each test case.

A consequence of the analysis is being able to validate the requirement to include a supporting lens in the ASP in addition to the sensor's built-in aperture. This decision will be informed by comparing the resulting signal margin with and without the additional lens collection area.

3.2 Analysis Methodology

The model is built from a series of combined efforts from Baker 1974 and The New SMAD, where Figure 3-1 shows a high-level overview of the parameters considered [3, 31]. The approach assumes that the auroral radiation is relatively monochromatic, meaning that it is produced over a very narrow band. We assume the green-line and red-line spectral channels have a width of 10-nm.

Note that the output of the AS7262 sensor is in units of counts/μW/cm^2. Considerations have been made in the analysis to determine the incident photon power required to constitute a single count for each of the six spectral channels. This allows a conversion from energy at the detector to counts registered at the sensor output.

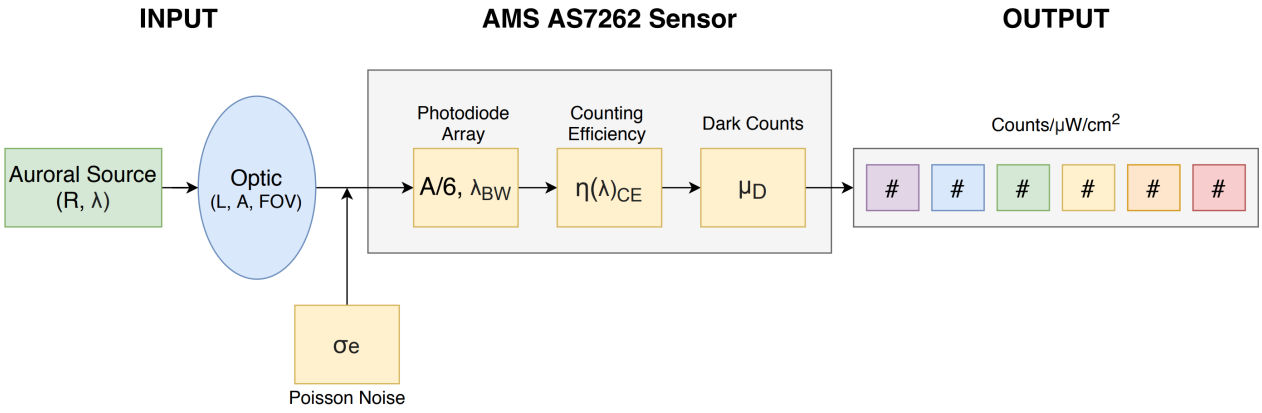

Figure 3-1: Mathematical model of single-pixel photodiode array

3.2.1 Calculating Power at the Detector

Referring back to Table 2.5 in Chapter 2, previous well-characterized measurements of auroral phenomena make up a list of source types within the AERO spectral photometer's observational range. Each species has a specified wavelength, λ in nm, and photon flux or Rayleigh radiance, ϕ_λ in units of Rayleigh [29, 3]. Recall that the Rayleigh is defined as 10^{10} photons m^2 $column^{-1}$ s^{-1}, and is often expressed in terms of kR. To begin the transformation from units of Rayleigh to power, we first convert photon flux to power radiance, L*, by

$$L^* = \frac{\phi_\lambda}{2\pi\lambda} \; x\; 10^{-13} \quad [\mathrm{W/cm^2/sr}] \tag{3.1}$$

where the source wavelength is in μm and is taken as the wavelength at the center peak of the spectral band [3]. Assuming our near-monochromatic auroral radiation is within a narrow wavelength band, Δ_λ, we define

$$L_\lambda = \frac{L^*}{\Delta_\lambda} \quad [\mathrm{W/cm^2/sr/\mu m}] \tag{3.2}$$

where L_λ is referred to as power spectral radiance. For a boxcar model of the auroral emission, the spectral channel width is estimated as 10 nm or 0.01 μm. In future work, use of models of spectral emission features as a function of wavelength are planned.

Next, we consider the effects of atmospheric transmissivity, τ_λ on power spectral radiance as radiation propagates to the detector's pixel. For space-based observations, we assume that this effect is negligible. Transmissivity effects are also heavily dependent on signal wavelength. Transmissivity affects the power spectral radiance by:

$$L_{up} = L_\lambda \tau_\lambda \quad [\mathrm{W/cm^2/sr/\mu m}] \tag{3.3}$$

where τ_λ is unitless. Next, we consider the sensor's bandwidth to account for detected power within the operational range.

$$L_{int}(\lambda) = \sum L_{up}\ (\lambda_i - \lambda_{i+1}) \quad [\mathrm{W/cm^2/sr}] \tag{3.4}$$

where $L_{int}(\lambda)$ is the integrated upwelling radiance, and the integrated terms inside the sum represent the sensor's bandwidth. For the AS7262, each channel has a bandwidth (FWHM) of $\pm$ 40 nm, meaning the upwelling radiance in our case is integrated over an 80 nm bandwidth. For L_{int}, the spectral dependence (μm) no longer appears in the denominator.

The sensor's FOV and spacecraft altitude affect the power observed by a single pixel derived from the integrated upwelling radiance. First, we consider the cross-track pixel dimension X and its ground resolution from the spacecraft orbit. To simplify the calculation, we only consider the pixel dimension as it is projected at nadir. A more detailed calculation would also consider ground resolution at the detector's maximum slant range and intervals in-between. The across-track ground pixel resolution is found with:

$$X = IFOV_x \times N \times \delta \times \frac{\pi}{180} \quad [\mathrm{m}] \tag{3.5}$$

where $IFOV$ is the instantaneous FOV in degrees, N is the number of samples and δ is the distance between the sensor aperture at the spacecraft and target observation in units of meters. The number of samples for AERO's measurement is one and δ represents the difference in altitude between the spectral photometer and the auroral F-region; δ is approximately 350 km at periapsis in the LEO orbit. The IFOV describes the width of one detector pixel. AERO's AS7262 sensor is an array of photodiodes and is considered a single-pixel detector. More complex instruments such as cameras or CCDs perform signal detection over multiple pixels and must take this term into consideration.

$$IFOV = \frac{Y_{max}}{R_s}\frac{180^\circ}{\pi} \quad [\mathrm{deg}] \tag{3.6}$$

where Y_{max} is the maximum ground sampling distance in meters and is defined by spatial resolution requirements of the detector. R_s is the spacecraft's slant range in units of meters and is defined by orbital geometry. Recall that we add a supporting

optic with a 20° FOV for each of AERO's optical sensors to meet the desire to be able to identify emission from individual arcs.

We also calculate the along-track ground pixel resolution, Y, for the purpose of defining radiated power from the projected ground pixel. This term is identical to the calculation made for the across-track pixel in Equation 3.6. For the purpose of this work, we assume that X and Y are equal.

Finally, the radiated power from the projected ground pixel, L, is found by

$$L = L_{int} \times X \times Y \quad [\text{W/sr}] \tag{3.7}$$

where L_{int} is in units of W cm^{-2} sr^{-1} and X and Y are both in terms of meters.

Perhaps the most important term in the analysis is the fraction of power radiated from the aurora incident at the sensor's aperture, P_{in}. Note that this is actually the power incident at the sensor's optic prior to entering the aperture.

$$P_{in} = \left(\frac{L}{\delta^2}\right)\left(\frac{D}{2}\right)^2 \pi \quad [\text{W}] \tag{3.8}$$

where δ is again the altitude between the sensor and the aurora, and D is the optic diameter in units of meters. In reality, incident power at the detector won't always align perfectly with the sensor's optical axis. Detected power at the aperture will fluctuate with field location relative to the spacecraft's position on-orbit, resulting in partial illumination of the sensor's detector by an auroral event. To compensate for this effect, the analysis considers an illumination factor that assumes varying percentages that represent detector coverage. For example, a 100% fill factor assumes that the sensor is fully illuminated by an auroral arc, where 10% assumes only a sliver of the sensor's area is illuminated. To determine the actual power received, P_{ill}, multiply the sensor power input by the illumination factor IF:

$$P_{ill} = P_{int} \times IF \quad [\text{W}] \tag{3.9}$$

3.2.2 Determining the Sensor's Signal-to-Noise Ratio

Energy collected by the sensor in a given integration period is found by

$$E = P_{ill}\ t_{int} \quad [\text{J}] \tag{3.10}$$

where t_{int} represents the AS7262 sensor's integration time. In the specification sheet, the minimum integration time is 2.8 ms and the maximum integration time is 255× 2.8 ms, or 714 ms. The manufacturer uses an integration time of 166 ms during their calibration test determining the [counts/μW/cm^2]. [1]. The maximum integration time of the sensor (t_{max}) is 714 ms. We may want to take measurements from auroral swaths over longer intervals. The spectral photometer does not have an electronic shutter, although it can drive a signal to sync with an external shutter. If the data can be rapidly read out, we can try to combine integration times, but still need at least one count detected per integration time. There is also a trade in increasing exposure time while maintaining high temporal and spatial resolution while moving in orbit. This affects the ability to extract meaningful structural information. It does not make sense for an exposure time to be much larger than $t_{int} = 1$ second in a LEO orbit. The spacecraft in LEO is moving at 7 km/s meaning that the sensor is quickly sweeping over a large amount of auroral structure. Intervals longer than 1 s may compromise the data such that it blurs information as the spacecraft moves along its trajectory, potentially preventing the ability to differentiate between individual arc structures.

We can apply Planck's law to determine the number of photons from the energy at the detector:

$$N_\gamma = \frac{E\lambda}{hc} \quad [\text{photons}] \tag{3.11}$$

where λ is the source wavelength in meters, h is Planck's constant (6.626×10^{-34} m^2 kg^{-1} s^{-1}) and c is the speed of light in vacuum at $3{\times}10^8$ m/s.

Radiometric analyses consider the detector's ability to convert incident photons to photogenerated carriers, or electrons, a term referred to as Quantum Efficiency

(QE). The QE of a detector is typically reported on a specification sheet; however, information regarding the device's quantum efficiency is not publicly available. This requires a modified approach for describing the sensor's ability to convert incident photon energy to counts at its output. Chapter 4 discusses an experimental setup in the lab that will enable us to better characterize the sensor. For the purpose of this work, we assume the sensor has a QE of 100% and discuss the effects of how varying the QE alters the sensor's minimum detectable signal in terms of resulting counts.

To find the number of available electrons from the incident photons N_γ,

$$N_e = N_\gamma \, QE \quad \text{[electrons]} \tag{3.12}$$

The Poisson, or photon, noise is a property inherent to light due to its quantum nature and is applied to the number of photocarriers generated by the incident photon.

$$\sigma_e = \sqrt{N_e} \quad \text{[electrons]} \tag{3.13}$$

The sensor's specification sheet provides a dark channel count (μ_D), or noise apparent on each channel when the sensor's aperture is capped. This value was derived with a gain setting of 64 and integration time set at 166 ms. μ_D is five counts for each of the six channels. We will confirm the sensor's dark count by replicating the test parameters in the sensor's specification sheet in lab. Note that the vendor also reports a typical value of counts, discussed further in Chapter 4, observed on all sensor channels when the sensor is illuminated with a source of 600 μW cm^{-2}. The dark count value was taken while the sensor gain was set at 16. We do not assume that the gain scales linearly, which makes it more complicated to use the reported illuminated counts and dark channel counts, since they were at different gain settings. Additional testing is needed to better understand dark counts as a function of the gain setting.

For the moment, we assume that μ_D of 5 counts is a usable value for sensor noise. We attempt to convert counts into energy.

$$P_{dark} = \mu_D \, \eta(\lambda)_{CE} \quad \text{[W]} \tag{3.14}$$

where μ_D is 5 counts from the sensor datasheet, and $\eta(\lambda)_{CE}$ is what we will call the 'counting sensitivity' in units of Watts per count. Based on the available sensor data, we estimate $7.83E^{-10}$ W/count. This is discussed in more detail in Section 3.2.3, and is based on the datasheet value of 45 counts/μW/cm^2, the area of the package, the 6 bands (the sensor area is smaller than the package dimensions of 4.5 mm by 4.7 mm, so this is an area that needs further investigation and updating), the information that the illuminating source was 600 μW/cm^2 and that the integration time for this test was t_{int} = 166 ms. In future work, we will obtain more detailed sensor information and test to assess whether this value is appropriate.

We convert from power (P_{dark}) to dark channel energy E_{dark}

$$E_{dark} = P_{dark}\, t_{int} \quad [\text{J}] \tag{3.15}$$

where t_{int} is 166 ms from the sensor's specificaion sheet. We then determine the number of photons present on the dark channels by applying Planck's law once more:

$$\gamma_{dark} = \frac{E_{dark}\lambda}{hc} \quad [\text{photons}] \tag{3.16}$$

where λ is assumed to be the source wavelength in meters; we use the center wavelength of the channel.

We then convert from dark channel photons to electrons:

$$\sigma_{dark} = \sqrt{\gamma_{dark}} \quad [\text{electrons}] \tag{3.17}$$

Finally, the total system noise is calculated by:

$$N_{tot} = \sqrt{\sigma_e^2 + \sigma_{dark}^2} \tag{3.18}$$

There will be additional terms for other noise sources, such as read noise, background noise from terrestrial interference, contributions from light reflected from the moon, etc. The process of calculating these terms is not trivial and is left as a future task.

In this work, we focus on whether the incident light from the aurora is strong enough to register as 1 count on the detector. Normally, a radiometric analysis would consider the SNR; however, we do not have enough information on the noise parameters of the detector to do so. To obtain the system's signal-to-noise ratio (SNR):

$$SNR = \frac{N_e}{N_{tot}} \tag{3.19}$$

3.2.3 Signal Margin

The publicly available datasheet for the spectral photometer does not contain detailed information about the device's noise sources or properties, such as dark current or ADC noise, that are typically accounted for in radiometric analyses, for example, for instruments that use CCDs. To manage this for an initial analysis, we use the sensor's counting sensitivity, $\eta(\lambda)_{CE}$, which is in terms of incident power to output counts, and the integration time during the manufactuer's calibration test to obtain energy required per count, and then compare the incident energy to the energy required per count to see if the signal is strong enough to be detected as 1 count.

The vendor datasheet reports that each sensor channel has raw data output of 45 counts/μW/cm^2. The vendor obtained this value when illuminating the sensor with a white LED broadband source with an irradiance of ~600μW/cm^2 and using an integration time of 166 ms. We infer that when they performed the test, they measured the sensor output for each of the channels of 27,000 counts, and they divided this by the known source irradiance to get 45 counts/μW/cm^2.

To ensure that the incidentt signal will at least cause a single count to register on the detector, we first determine the amount of power incident on the detector that causes a single count on the sensor's output. We refer to this as the sensor's 'count sensitivity.'

The sensor package dimensions, provided in Table 2.4 give a total package area A_{det} as 21.15 mm^2. The spectral photometer is an array of photodiodes, meaning that it is necessary to account for each element's individual area. The individual

area values are not provided by the vendor. To account for each element, we divide A_{det} by 6, or the total number of photodiodes. This simplified assumption does not account for the sensor being smaller than the package size, or the spacing between the elements. We then determine the sensor's counting sensitivity by

$$\eta(\lambda)_{C,\mu} = \frac{S_{test} A_{phot}}{C_{meas}} \quad [\mu\text{W/count}] \tag{3.20}$$

where S_{test} is the LED irradiance, A_{phot} is the photodiode area in cm^2 and C_{meas} is 27,000 counts. This is used to calculate power per count by:

$$\eta(\lambda)_C = \eta(\lambda)_{C,\mu} \times 10^{-6} = 7.83 \times 10^{-10} \quad [\text{W/count}] \tag{3.21}$$

Determining the number of counts detected from the incident auroral source, we first translate power per count to energy per count by multiplying the counting sensitivity by the fixed integration time:

$$E_{count} = \eta(\lambda)_C \; t_{int} \quad [\text{J/counts}] \tag{3.22}$$

where t_{int} is 166 ms. The energy per sensor read for the maximum integration time is then found by:

$$E = P_{ill} \times t_{int,max} \quad [\text{J}] \tag{3.23}$$

where $t_{int,max}$ is 714 ms and P_{ill} is in units of Watts. Last, we determine the number of sensed counts at the detector by:

$$Counts = \frac{E}{E_{count}} \quad [\text{Counts}] \tag{3.24}$$

If we need to achieve at least one count to detect the aurora, the count margin is:

$$Margin = Counts - 1 \quad [\text{counts}] \tag{3.25}$$

Another consideration is the likelihood of sensor saturation due to a particularly

bright auroral arc. The maximum number of counts the detector can handle prior to reaching its saturation point is determined by the ADC. The AS7262 sensor has a 16-bit ADC meaning it can detect signals that correspond to 65,536 counts before it will saturate. It is unknown at this time how any internal gain control on the sensor can be used in handling saturation.

THIS PAGE INTENTIONALLY LEFT BLANK

Chapter 4

Analysis Results and Summary

4.1 Analysis Results

The objective of the radiometric model is to assess sensor performance for several different scenarios. Table 4.1 defines the complete list of parameters considered for this assessment. The reference case is defined in Table 4.4, and shows the parameter list used for each test case. Table 4.3 provides results from the reference case that can be compared with results from other cases. Note that power at the detector (P_{in}) and total detector illuminated power (P_{ill}) are equivalent. This is due to the assumption in the baseline reference case that the full detector area is illuminated by an auroral arc, meaning that the IF is 100%. A similar relationship is observed between the number of available photons (N_γ) and electrons (N_e) due to the initial assumption for thie work that the sensor has a QE of 100%.

It is shown that in baseline reference configuration (Table 4.3), the resulting signal margin is 0.5, meaning that, with these assumptions, the sensor is just able to detect (by registering 1 count) an auroral event with Rayleigh radiance of 100 kR. We next show how tuning the different parameter 'knobs' affect the resulting margin. We attempt to find a case that maximizes margin. We use bold font to help make any results that vary from the results in the baseline reference case stand out for easy identification.

Integrated upwelling radiance is a key parameter for comparing the first part of the

Table 4.1: Morphological matrix of test parameters used for analysis cases

Parameter	Choice 1	Choice 2	Choice 3	Choice 4
Wavelength (nm)	550	630	-	-
Rayleigh Radiance (kR)	1	10	100	1000
Spacecraft Altitude (km)	450	650	-	-
Illumination Factor (%)	100%	80%	50%	10%
Supporting Lens Diameter (cm)	N/A	0.5	1	2
Sensor Quantum Efficiency	100%	90%	75%	50%

Table 4.2: Test parameters that define the baseline reference case

Parameter	Value
Wavelength (nm)	557.7
Rayleigh Radiance (kR)	100
Spacecraft Altitude (km)	450
Integration Time (ms)	714
Illumination Factor (%)	100
Supporting Lens Diameter (cm)	1
Sensor Quantum Efficiency	100%

model's output with the literature. To assess our model's performance, we compare the computed (L_{int}) from our baseline reference case with previous work done by Shaw with respect to green-line emission at 557.7 nm [28]. The model successfully computes an upwelling radiance value to within 0.02. This small difference is likely due to rounding error, use of different values of atmospheric transmissivity, or our estimated width of the auroral spectra line.

4.1.1 Minimum Detectable Signal

Mission requirements state that the spectral photometer shall be able to discern a 5 kR auroral signal from sensor and background noise. Table 4.5 shows the results for this test scenario; the only difference between this case and the baseline reference case

Table 4.3: Baseline Reference Case Results

Parameter	Value	Units
Power Radiance (L^*)	2.85E-09	$W/cm^2/sr$
Integrated Upwelling Radiance (L_{int})	2.85E-05	$W/m^2/sr$
Radiated Power from Ground Pixel (L)	4.26E+05	W/sr
Input Power at Detector (P_{in})	2.73E-10	W
Actual Power at Sensor (P_{ill})	2.73E-10	W
Energy Per Integration (E)	1.95E-10	J
Resulting Photons (N_{gamma})	3.65E+08	Photons
Resulting Noise Electrons (σ_c)	1.91E+04	Electrons
Dark Channel Electrons (σ_{dark})	8.86E+04	Electrons
Output Counts	1.50	Counts
Margin	0.5	Counts

Table 4.4: Comparing model results with previously work from Shaw for green-line emission [28]

IBC Level	Rayleigh	Radiance (Shaw)	Radiance (AERO)	Units
I	1 kR	2.833 x 10^{-7}	2.854x10^{-7}	$W/m^2/sr$
II	10 kR	2.833 x 10^{-6}	2.854x10^{-6}	$W/m^2/sr$
III	100 kR	2.833 x 10^{-5}	2.854x10^{-5}	$W/m^2/sr$
IV	1000 kR	2.833 x 10^{-4}	2.854x10^{-4}	$W/m^2/sr$

is that we decrease Rayleigh radiance to 5 kR from 100 kR. The margin is negative and therefore undetectable, as the energy at the detector is below the value that would generate 1 count. The inability to generate 1 count for the 5 kR case using the other baseline reference parameters is expected, considering the findings in the baseline reference case with higher auroral radiance of 100 kR.

4.1.2 Source Wavelength

We compare a signal received from each of our two primary targets, green-line (557 nm) and red-line (630 nm) auroral emission. We observe minimal effects on the

Table 4.5: Results for 5 kR case

Parameter	Value	Units
Power Radiance (L^*)	1.43E-10	$W/cm^2/sr$
Integrated Upwelling Radiance (L_{int})	1.43E-06	$W/m^2/sr$
Radiated Power from Ground Pixel (L)	2.13E+04	W/sr
Input Power at Detector (P_{in})	1.37E-11	W
Actual Power at Sensor (P_{ill})	1.37E-11	W
Energy Per Integration (E)	9.75E-12	J
Output Counts	0.07	Counts
Margin	-0.93	Counts

resulting signal margin, where an increase in wavelength to 630 nm results in decreased margin. This is expected, as we are using the same input Rayleigh values for each line, and the sensor's counts/$\mu W/cm^2$ are the same for both channels. The wavelength difference affects the power radiance.

Table 4.6: Comparing Results for green and red auroral source wavelengths

Parameter	557.7nm	**630 nm**	Units
Power Radiance (L^*)	2.85E-09	**2.53E-09**	$W/cm^2/sr$
Integrated Upwelling Radiance (L_{int})	2.85E-05	**2.53E-05**	$W/m^2/sr$
Radiated Power from Ground Pixel (L)	4.26E+05	**3.77E+05**	W/sr
Input Power at Detector (P_{in})	2.73E-10	**2.42E-10**	W
Actual Power at Sensor (P_{ill})	2.73E-10	**2.42E-10**	W
Energy Per Integration (E)	1.95E-10	**1.73E-10**	J
Output Counts	1.5	**1.33**	Counts
Margin	0.5	**0.33**	Counts

4.1.3 Source Rayleigh Radiance

Next, we compare the signal margin as a function of varied source radiance in units of Rayleigh. Per Table 2.1, the maximum Rayleigh radiance we anticipate observing

within the spectral photometer's observation band is 800 kR ($N_2$1P), while the lowest we anticipate seeing is 2 kR (O^1D). Results from the 1, 100, and 1000 kR parameters with the baseline reference case are shown in Table 4.7, and results from the ($N_2$1P) emitter at 800 kR are found in Table 4.8. We observe that, as expected, changes in source radiance contribute significantly to changes in signal margin. Margin is not positive until the source is close to 100 kR with our initial set of assumptions.

Table 4.7: Comparing Results for varied source Rayleigh radiance

Parameter	100 kR	**1 kR**	**10 kR**	**1000 kR**	Units
Power Radiance (L^*)	2.85E-09	**2.85E-11**	**2.85E-10**	**2.85E-08**	$W/cm^2/sr$
Integrated Upwelling Radiance (L_{int})	2.85E-05	**2.85E-07**	**2.85E-06**	**2.85E-04**	$W/m^2/sr$
Radiated Power from Ground Pixel (L)	4.26E+05	**4.26E+03**	**4.26E+04**	**4.26E+06**	W/sr
Input Power at Detector (P_{in})	2.73E-10	**2.73E-12**	**2.73E-11**	**2.73E-09**	W
Actual Power at Sensor (P_{ill})	2.73E-10	**2.73E-12**	**2.73E-11**	**2.73E-09**	W
Energy Per Integration (E)	1.95E-10	**1.95E-12**	**1.95E-11**	**1.95E-09**	W
Output Counts	1.5	**0.01**	**0.15**	**15.0**	Counts
Margin	0.5	**-0.99**	**-0.85**	**14.0**	Counts

4.1.4 Spacecraft Altitude

Next, we compare the signal margin when the spacecraft is at 450 km at periapsis, compared with an altitude of 650 km at apoapsis. Results shown in Table 4.9 indicate that the change in altitude has little effect on the resulting signal margin. It is possible that larger slant ranges may be encountered on orbit. The notable change occurs on the radiated power from the projected ground pixel (L). The increase may seem odd,

Table 4.8: Comparing Results for brightest expected signal for visible sensor

Parameter	100 kR	**880 kR**	Units
Power Radiance (L^*)	2.85E-09	**2.51E-08**	$W/cm^2/sr$
Integrated Upwelling Radiance (L_{int})	2.85E-05	**2.51E-04**	$W/m^2/sr$
Radiated Power from Ground Pixel (L)	4.26E+05	**3.75E+06**	W/sr
Input Power at Detector (P_{in})	2.73E-10	**2.40E-09**	W
Actual Power at Sensor (P_{ill})	2.73E-10	**2.40E-09**	W
Energy Per Integration (E)	1.95E-10	**1.72E-09**	W
Output Counts	1.5	**13.2**	Counts
Margin	0.5	**12.2**	Counts

but it is because at a higher altitude, the 'ground resolution' is larger at a higher altitude, and we are assuming that the auroral signal is in the full FOV.

Table 4.9: Results from change in spacecraft altitude

Parameter	450 km	**650 km**	Units
Power Radiance (L^*)	2.85E-09	2.85E-09	$W/cm^2/sr$
Integrated Upwelling Radiance (L_{int})	2.85E-05	2.85E-05	$W/m^2/sr$
Radiated Power from Ground Pixel (L)	4.26E+05	**1.05E+06**	W/sr
Input Power at Detector (P_{in})	2.73E-10	2.73E-10	W
Actual Power at Sensor (P_{ill})	2.73E-10	2.73E-10	W
Energy Per Integration (E)	1.95E-10	1.95E-10	W
Output Counts	1.5	1.5	Counts
Margin	0.5	0.5	Counts

4.1.5 Illumination Factor

The IF is a percent factor directly multiplied to the input power at the detector to represent an area of detector coverage. We observe the anticipated result that when the sensor is not fully illuminated by an auroral event, it receives less power and thus experiences a decrease in signal margin. With less than 80% IF the baseline reference

case margin becomes negative. The IF results for are presented in Table 4.10.

Table 4.10: Results from variable detector coverage

Parameter	100%	**80%**	**50%**	**10%**	Units
Power Radiance (L^*)	2.85E-09	2.85E-09	2.85E-09	2.85E-09	$W/cm^2/sr$
Integrated Upwelling Radiance (L_{int})	2.85E-05	2.85E-05	2.85E-05	2.85E-05	$W/m^2/sr$
Radiated Power from Ground Pixel (L)	4.26E+05	4.26E+05	4.26E+05	4.26E+05	W/sr
Input Power at Detector (P_{in})	2.73E-10	2.73E-10	2.73E-10	2.73E-10	W
Actual Power at Sensor (P_{ill})	2.73E-10	**2.18E-10**	**1.37E-10**	**2.73E-11**	W
Energy Per Integration (E)	1.95E-10	**1.56E-10**	**9.75E-10**	**1.95E-11**	W
Output Counts	1.5	**1.2**	**0.75**	**0.15**	Counts
Margin	0.5	**0.2**	**-0.25**	**-0.85**	Counts

4.1.6 Supporting Lens

Next we evaluate the contributions from increasing the aperture diameter of the supporting lens. Here the baseline reference case (diameter of 1 cm) is compared to the signal received if there were no lens in place. Recall that the AS7262 sensor has a built-in aperture with diameter of 0.75 mm. We find that the additional aperture area is necessary in increasing the input power at the detector and thus the number of collected photons. We also observe that varying the lens diameter has a significant affect on the resulting margin.

4.1.7 Sensor Quantum Efficiency

Finally, we consider the effects on signal margin with decreased quantum efficiency, as we initially assume 100%. We recognize that this estimate is a best-case value and is likely not an accurate representation of the performance of our COTS component.

Table 4.11: Results from change support lens diameter

Parameter	1 cm	**0.075 cm**	**0.5 cm**	**2 cm**	Units
Power Radiance (L^*)	2.85E-09	2.85E-09	2.85E-09	2.85E-09	$W/cm^2/sr$
Integrated Upwelling Radiance (L_{int})	2.85E-05	2.85E-05	2.85E-05	2.85E-05	$W/m^2/sr$
Radiated Power from Ground Pixel (L)	4.26E+05	4.26E+05	4.26E+05	4.26E+05	W/sr
Input Power at Detector (P_{in})	2.73E-10	**1.54E-12**	**6.83E-11**	**1.09E-09**	W
Actual Power at Sensor (P_{ill})	2.73E-10	**1.54E-12**	**6.83E-11**	**1.09E-09**	W
Energy Per Integration (E)	1.95E-10	**1.10E-12**	**4.87E-11**	**7.80E-10**	W
Output Counts	1.5	**0.01**	**0.37**	**6.0**	Counts
Margin	0.5	**-0.99**	**-0.63**	**5.00**	Counts

We expect decreased performance with QE, and would desire a QE that is greater than 90% for the green-line and red-line bands.

4.2 Thesis Summary

In conclusion, from our initial assessment we have found few cases when the performance of the AMS AS7262 spectral photometer suffices to meet the sensor's minimum detection threshold for the target events in its current configuration. We find that it may be able to detect auroral events with high-levels of intensity (800 - 1000 kR). These results indicate that further analysis is necessary to confidently confirm the sensor's performance at lower levels such as 5 kR, and we may need to consider modifying the sensor's front-end optic or possibly reconsidering the sensor itself.

Other interesting observations resulted from this work, such as identifying parameters that have substantial or no impact on the resulting signal margin. For example, we find that altering spacecraft altitude, exposure time, and quantum efficiency have less of an effect on the resulting number of counts detected, while higher levels of

source intensity and larger aperture diameters generate substantial change. We observe that for our baseline reference case with radiance of 100 kR, the sensor's signal margin is 0.5. In the case of 1000 kR, the margin increases to 14 detected counts. Likewise, the margin changes from 0.5 to 6 when increasing lens diameter to 2 cm from 1 cm.

We find that from our defined test parameters in Table 4.1, the only instances when signal margins increase above the noise threshold are when the source Rayleigh radiance is substantial, at over 100 kR. The target green and red-line auroral events (at 557.7 nm and 630 nm) are observed to have intensities of 100 kR and 2-100 kR (see Table 2.1) respectively. By this metric, our initial assessment shows that we are unable to observe our target source with the AS7262 sensor in its current configuration and are therefore unable to satisfy the mission design requirement. We find that the minimum detectable signal, being able to generate a single count, occurs when Rayleigh radiance is approximately 100 kR.

Outside of adjusting the source intensity, which we have no control over, we find that the two parameters having the most impact on the resulting margin are the diameter of the supporting lens and its FOV. The FOV was intentionally excluded from the set of test parameters as this value is fixed by a of the mission's science requirements. Nonetheless, we find that by increasing the FOV of the supporting lens from 20° to 73° (full cone) we achieve a signal margin of 0, meaning we can achieve 1 count at the detector with a 5 kR source. Increasing the size of the supporting optic poses a structural design trade given that the lenses are mounted in cutouts in the spacecraft wall. Increasing lens diameter reduces the amount of thermal radiating area available on the spacecraft's structural frame for heat management. This is relevant because AERO's primary VS payload draws a substantial amount of power for a 6U CubeSat (35W peak power during data acquisition mode), making reducing available radiating area an important design trade.

We find that adjusting spacecraft altitude while remaining in LEO does not significantly impact the margin.

It is shown that when adjusting the illumination factor from 100% to only 10%

detector area coverage, the signal margin decreases from 0.5 to -0.85. Whether the FOV of the sensor is illuminated by an auroral event will impact the ability of the sensor to make a measurable detection.

While this thesis shows that the configuration or choice of the currently selected sensor may need reconsideration, the model created to perform this radiometric analysis serves as a useful tool for evaluating the behavior of an auroral imaging sensor. The model can be easily adapted to include effects from other terms such as additional noise (e.g., readout, background terrestrial interference), transmission loss from optics, and known values of quantum efficiency.

Chapter 5

Contributions and Future Work

5.1 Thesis Contributions

Contributions of this thesis include:

- Development of an easily adaptable radiometric model that computes the minimum detectable signal and signal-to-noise ratio of an auroral imager.
- A detailed assessment of the AMS AS7262 sensor's performance behavior given a set of defined mission parameters.
- Increased understanding of how a set of case parameters impact the performance of an auroral sensor.
- Informing critical design considerations for ASP component selection.
- A tool for verification of the sensor's performance against defined mission requirements by analysis.

5.2 Planned Laboratory Tests

There are a series of laboratory tests planned to assess the sensor's performance. Unfortunately, the effects of COVID-19 prohibited any test progress and thus they are left as future work. For brevity, the high-level objectives of each test can be found

in this section. Note that all but the vacuum survivability test would take place in a dark room on MIT's campus. The simplified block diagram shown in Figure 5-1 shows the order of operations for the laboratory assessments.
The objectives of the planned laboratory test are as follows:

- Component functional test: assess baseline sensor operation after receiving from shipping and handling to confirm that there is no damage. This is completed by simply commanding the sensor to take data from a known source and confirming that there are registered output counts on appropriate channels. Figure 5-9 shows an example of the sensor's output when receiving full (100%), continuous illumination from a white Plusivo kit LED for 26 samples with an integration time of 166 ms. The second iteration of functional testing post vacuum will provide a comparison of the sensor's performance before and after exposure in the test chamber.

- Vacuum survivability: determine the sensor's ability to survive vacuum exposure. The sensor is not space qualified and as such its ability to survive launch and operation on-orbit is currently unknown. This serves as the first step in space qualifying the sensor. The sensor has been placed (powered off) in a small chamber in the Space Systems Lab (see Figure 5-2). Registered output counts shown in Figure 5-9 are results from functional testing post-vacuum, though a detailed comparison of results before and after exposure are not part of this work.

- Verification of specification sheet: replicate test parameters from sensor specification sheet to validate sensor performance with respect to quoted values from vendor. Figure 5-3 shows the test setup where the source is a known emitter with irradiance of $600\mu\text{W/cm}^2$.

- Assessment of temperature effects: assess sensor's sensitivity to incident source emission as a function of fluctuating temperature. The sensor will be powered on and commanded to take data while in a thermal vacuum chamber. This is

broken into two test scenarios: the first where the sensor's aperture is capped to assess fluctuation of dark channel counts as a function temperature, and the second with the presence of a source with known irradiance.

- Deriving sensor efficiency: test the sensor's performance with a well calibrated source to extract an efficiency factor. Figure 5-4 shows the test configuration, where a temperature calibrated diode and integrating sphere are used to produce an even source with known intensity. A photodiode positioned at an input port on the integrating sphere reads intensity from the source diode, and then feeds this value through a picoammeter to determine source flux. This provides a direct comparison between known source flux and flux registered at the sensor input and serves to empirically derive the sensor's counting sensitivity, thus verifying the efficiency value calculated by the radiometric model.

- Full optical chain: assess the performance of the sensor with full optical chain in-the-loop. Figure 5-5 shows the test configuration for validating the performance of both the AS7262 sensor as well as its supporting lens. A variable attenuator is used to simulate distance between the signal and source by attenuating source intensity prior to it reaching the sensor's aperture. Due to the impact of COVID-19, a heavily simplified version of this test configuration is shown in Figure 5-6 where a red LED is slowly incremented away from the sensor's aperture. Preliminary results from this test are shown in Figure 5-8

5.3 Additional Future Tasks

We list some additional tasks toward a full assessment of the sensor's performance:

- Adapt the radiometric model to consider noise contributions from Earth and moon background interference during acquisition periods.

- Determining a method for calculating transmission loss imposed by sensor optics and replacing current estimated values in model.

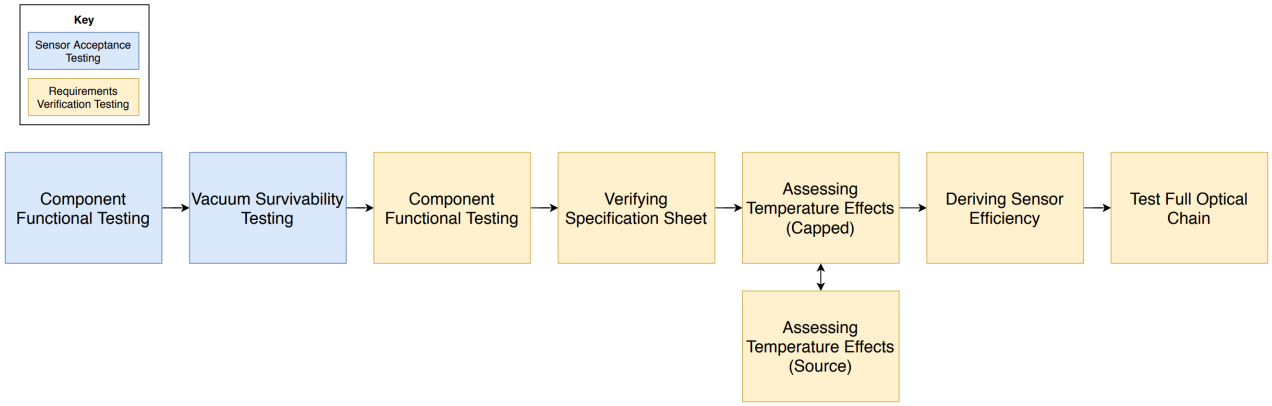

Figure 5-1: High-level overview of sensor test flow diagram.

- Completing laboratory testing to assess actual sensor performance, to verify analysis results and values listed in the sensor specification sheet, and to empirically derive counting efficiency.
- Determine the minimum number of acceptable samples we require from the sensor flying over an auroral arc to confidently claim observation of an auroral event.
- Determine green-line and red-line auroral spectral shapes and defined channel widths to replace rectangular function placeholder. Adapt model to consider realistic spectral shape as an input.

Additional tasks for qualifying the sensor for flight:

- Laboratory testing to determine noise contributions as a function of temperature.
- Determine the behavior of the sensor's gain as a function of temperature. The current assumption is that the gain behaves linearly.
- Thermal vacuum testing to assess sensor survivability in the space environment.
- Laboratory testing of the full optical chain to assess alignment and insertion loss from sensor optic.

Figure 5-2: AS7262 placed unpowered in the SSL bell jar. Chamber pumped down to 19.1 mTorr

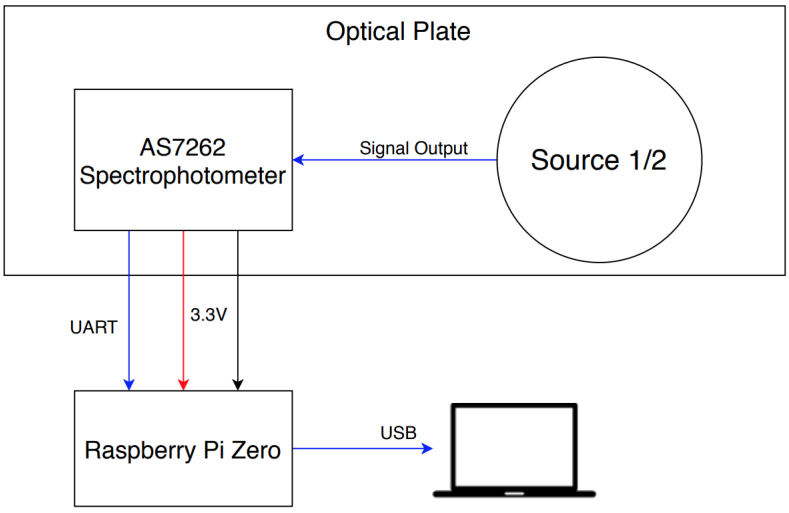

Figure 5-3: Block diagram of specification sheet verification test.

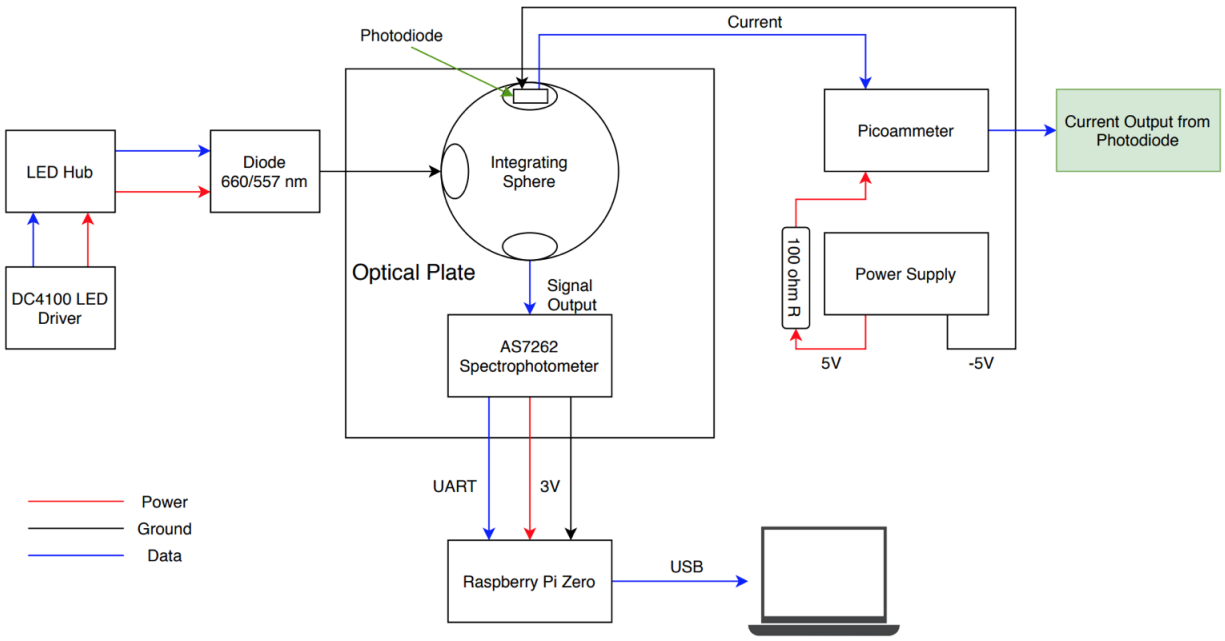

Figure 5-4: Test diagram of laboratory setup to extract sensor counting efficiency.

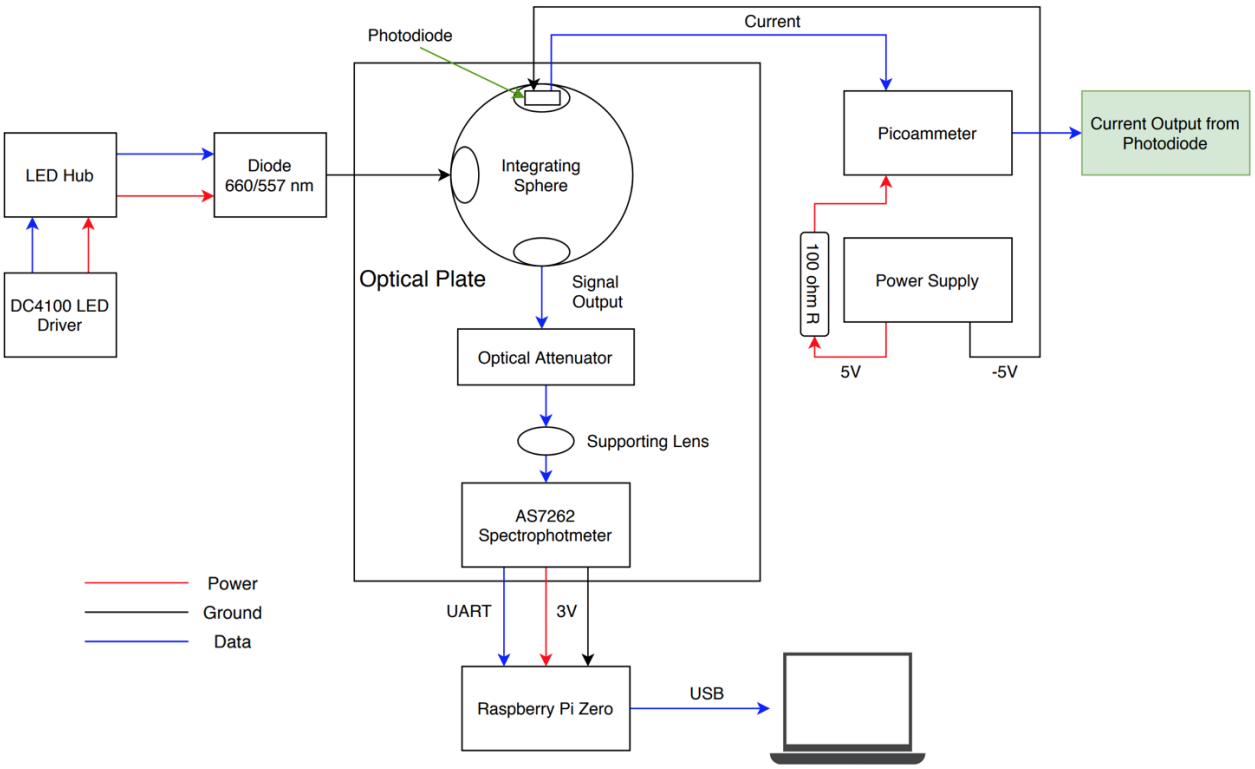

Figure 5-5: Test diagram of laboratory test to verify performance of full optical chain.

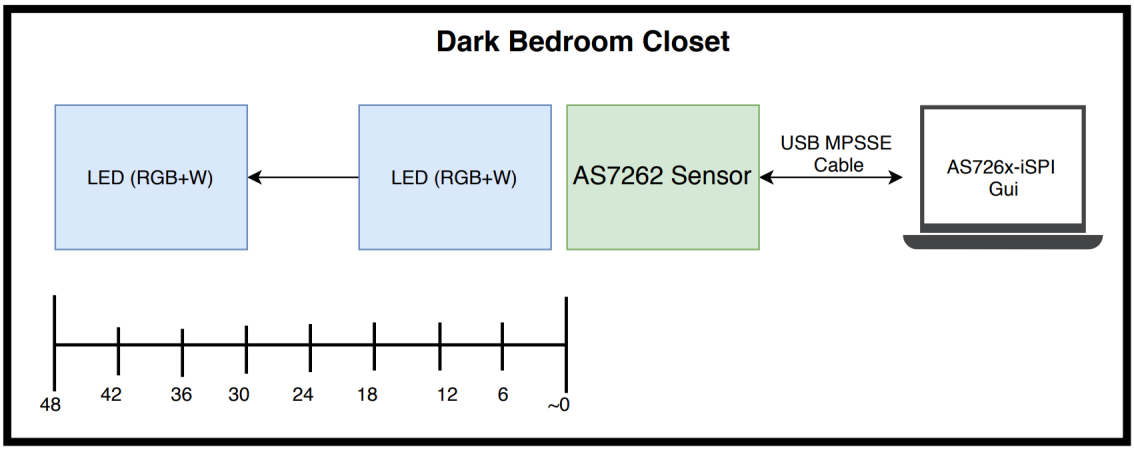

Figure 5-6: Test diagram of 'step' test in dark closet.

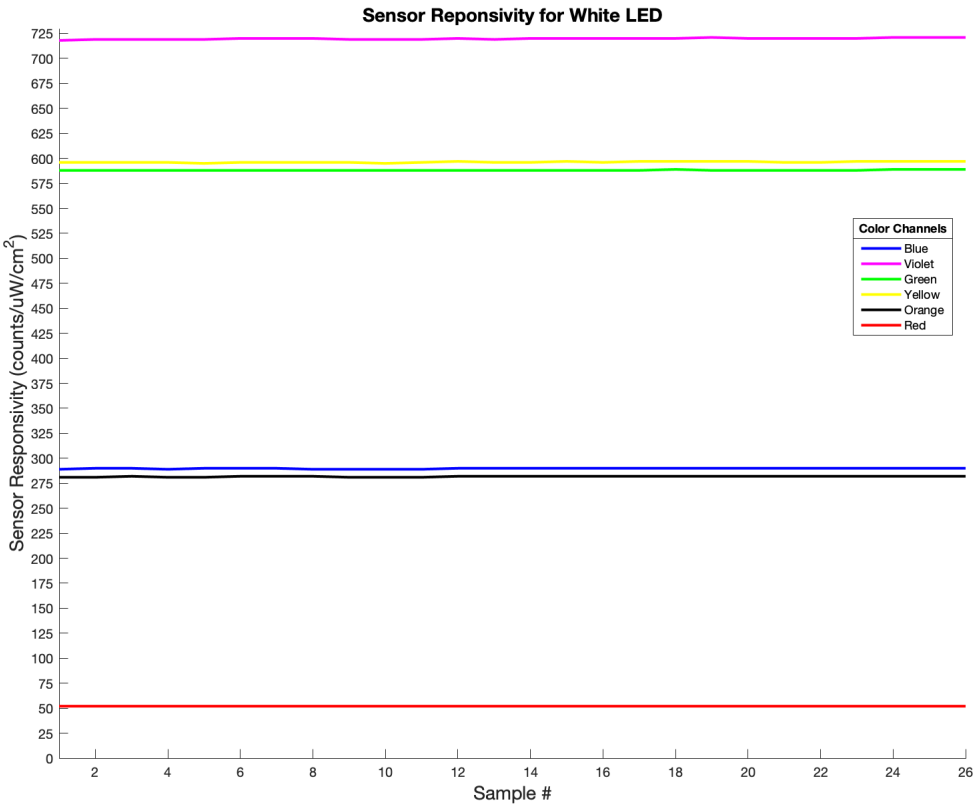

Figure 5-7: AS7262 channel response from full illumination by a white Plusivo kit LED with integration time of 166 ms

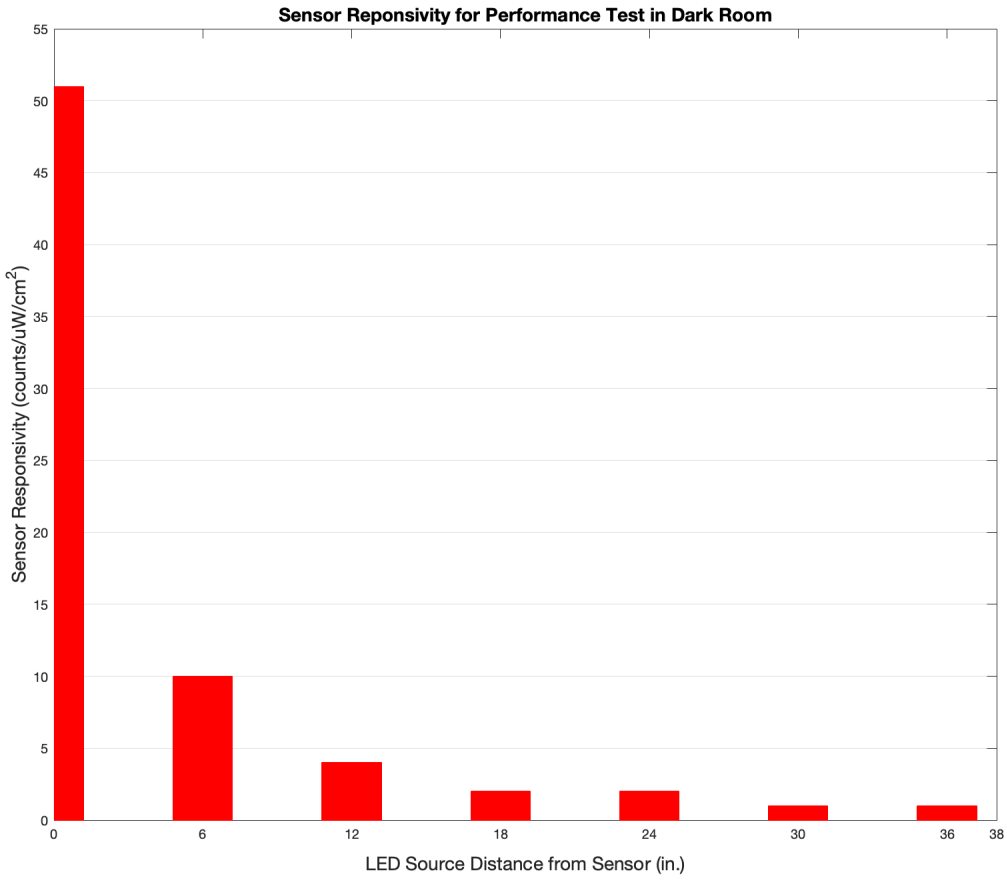

Figure 5-8: Sensor output from 'step' test in dark closet.

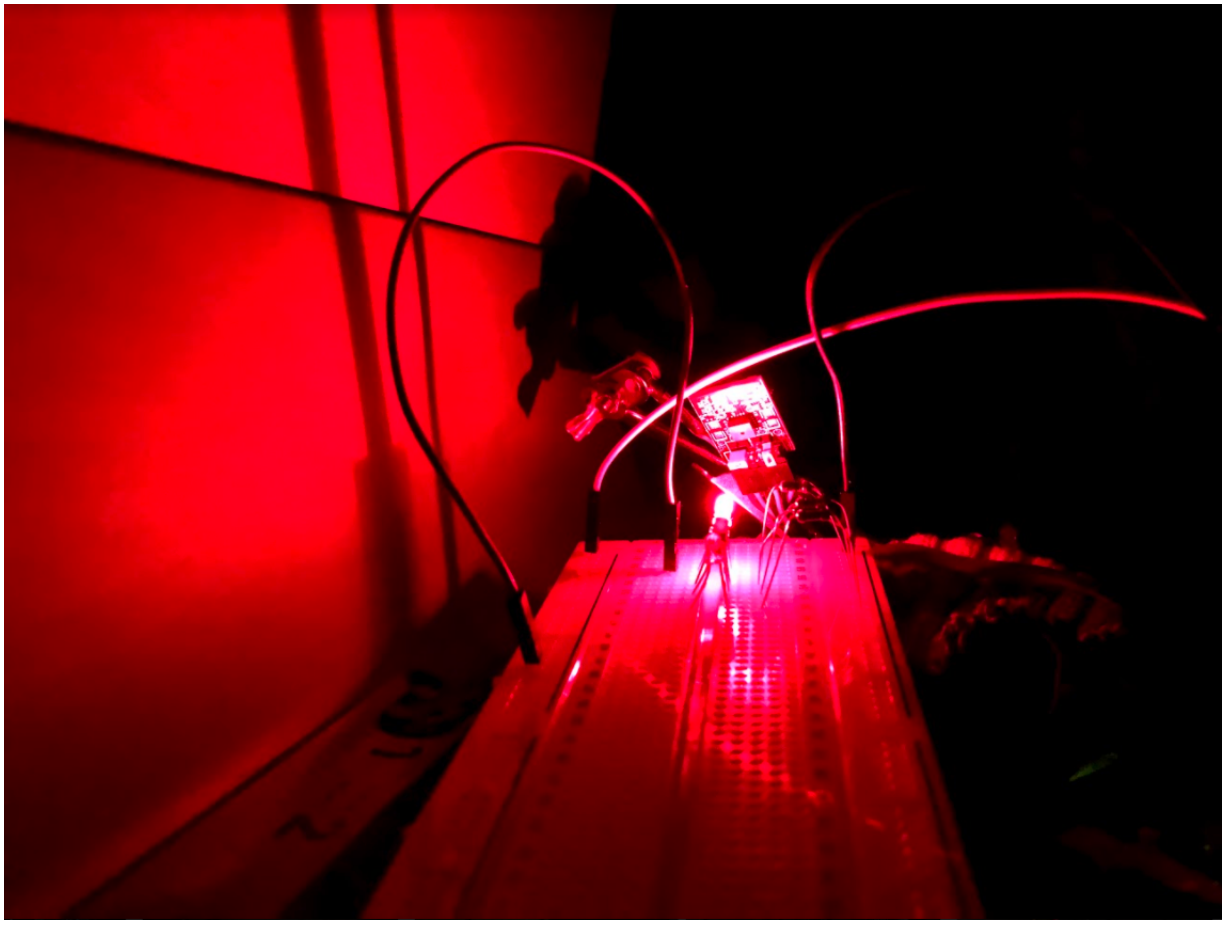

Figure 5-9: AS7262 channel fully illuminated by a red LED in dark closet. Results shown in Figure 5-8.

Bibliography

[1] AMS AG. As7262 consumer grade smart 6-channel vis sensor. https://ams.com/documents/20143/36005/AS7262$_D$S000486$_2$ − 00.*pdf*/0031*f*605−5629−*e*030−73*b*2−*f*365*f*d36*a*43*b*, 2017.*originaldocumentfromAMSAG*.

[2] Andor. Radiometry and photometry explained.

[3] Doran J. Baker. Rayleigh, the unit for light radiance. *Appl. Opt.*, 13(9):2160–2163, Sep 1974.

[4] G. Branduardi-Raymont, Dhiren Kataria, D'Auvion Walton, A. Fazakerley, and Andrew Coates. Exact: A study of the earth's aurora using a cubesat. 09 2010.

[5] J. W. Chamberlain. *Physics of the Aurora and Airglow*. Academic Press, New York, 1961.

[6] James W. Cutler and Hasan Bahcivan. Radio aurora explorer: A mission overview. *Journal of Spacecraft and Rockets*, 51(1):39–47, 2014.

[7] Philip J. Erickson, Geoffrey Crew, Michael Hecht, Mary Knapp, Frank D. Lind, and Ryan Volz. Aero: Auroral emissions radio observer. *Proceedings of the AIAA/USU Conference on Small Satellites*, August 2018. SSC18-WKVI-04. https://digitalcommons.usu.edu/cgi/viewcontent.cgi?article=4265context=sma

[8] ESA. Andesite 6u cubesat auroral plasma science mission of boston university, 202o.

[9] Y.I. Feldstein and G.V. Starkov. Dynamics of auroral belt and polar geomagnetic disturbances. *Planetary and Space Science*, 15(2):209 – 229, 1967.

[10] Rob Garner. Nasa's newly rediscovered image mission provided key aurora research, 2018.

[11] David Gubbins and Emilio Herrero-Bervera. *Encyclopedia of Geomagnetism and Paleomagnetism*. Springer, 2007.

[12] D.M. Hunten, F.E. Roach, and J.W. Chamberlain. A photometric unit for the airglow and aurora. *Journal of Atmospheric and Terrestrial Physics*, 8(6):345 – 346, 1956.

[13] Alister Vallance Jones. *Aurora*. D. Reidel Publishing Company, 1974.

[14] Kari Kaila. Optical measurements of aurora. University Lecture, 2011.

[15] Mary Knapp. Aero-vista l0 / l1 requirements. Mission requirements documentation for AERO-VISTA mission, 2019.

[16] Mary Knapp, Ryan Volz, Frank D. Lind, Frank C. Robey, Alan Fenn, Kerry Johnson, Mark Silver, Alex Morris, and Sarah Klein. *HF Vector Sensor for Radio Astronomy: Ground Testing Results.*

[17] J. Labelle. Spontaneous radio frequency emissions from natural aurora. *NATO Technical Report RTO-TR-IST-051*, 2006.

[18] J. Labelle and R.R Anderson. Ground-level detection of auroral kilometric radiation. *Geophys. Res.*, 2011.

[19] G. Le, J. A. Slavin, and R. J. Strangeway. Space technology 5 observations of the imbalance of regions 1 and 2 field-aligned currents and its implication to the cross-polar cap pedersen currents. *Journal of Geophysical Research: Space Physics*, 115(A7), 2010.

[20] M12 Lenses. Pt-02120 2.1mm, f2.2 board lens.

[21] Frank D. Lind, Philip J. Erickson, Hecht Michael, and Mary Knapp. Aero & vista: Demonstrating hf radio interferometry with vector sensors. *Proceedings of the AIAA/USU Conference on Small Satellites*, August 2019. SSC19-WKV-09. https://digitalcommons.usu.edu/smallsat/2019/all2019/96/.

[22] nasa_{2019}. Geotail, august 2019.

[23] Larry J. Paxton and Ching-I. Meng. Auroral imaging and space-based optical remote sensing. 1999.

[24] Frank C. Robey, Mary Knapp, Alan J. Feen, Mark Silver, Kerry Johnson, , Frank D. Lind, Ryan Volz, Sara Seager, and Farshid Neylon-Azad. High frequency (hf) radio astronomy from a small satellite. *Proceedings of the AIAA/USU Conference on Small Satellites*, August 2016. SSC16-XI-03. https://digitalcommons.usu.edu/smallsat/2016/TS11SciPayload1/3/.

[25] R. M. Robinson and R. R. Vondrak. Validation of techniques for space based remote sensing of auroral precipitation and its ionospheric effects. *Space Science Reviews*, 69(3):331–407, 1994.

[26] Randy Russell. Charged particle motion in earth's magnetosphere auroral colors and spectra.

[27] Paul Schlyter. Radiometry and photometry in astronomy.

[28] Joseph A. Shaw, Jesse M. Way, Nathan J. Pust, Paul W. Nugent, Hans Coate, and Daniel Balster. Optical aurora detectors: using natural optics to motivate education and outreach. In *Education and Training in Optics and Photonics*, page ESB4. Optical Society of America, 2009.

[29] Trond Trondsen. High spatial and temporal resolution auroral imaging - ph.d. dissertation. 01 1998.

[30] Mark Wade. Themis, 2019.

[31] J. R. Wertz, D. F. Everett, and J. J. Puschell. *Space mission engineering: The new SMAD*. Microcosm Press, 2011.

[32] Holly Zell. Themis-artemis overview, 2020.